People`s Democratic Republic of Algeria
Ministry of Higher Education and Scientific Research
University of Echahid Hamma Lakhdar - El Oued
Faculty of Technology
Department of Electrical Engineering

Dissertation

ACADEMIC MASTER

Domain: Science and Technology

Division: **Electrical Engineering**

Specialty: **Telecommunication Systems**

Presented by:

1. **Raoinak Melik,**
2. **Nabila Habita**

Entitled:

Optimizing the Photovoltaic Performance of Lead-Free Perovskite Solar Cells through Numerical Simulation

Dissertation Submitted in Partial Fulfillment of the Requirements for the Master Degree in **Telecommunication Systems**

Publicly defended in: **28 /05 /2025**

Board of Examiners:

Dr. Fritah Abdallah	**Chairman**
Dr. Tinedert Imad Eddine	**Supervisor**
Dr. Bellili Nour El Imane	**Examiner**

Academic Year: 2024/2025

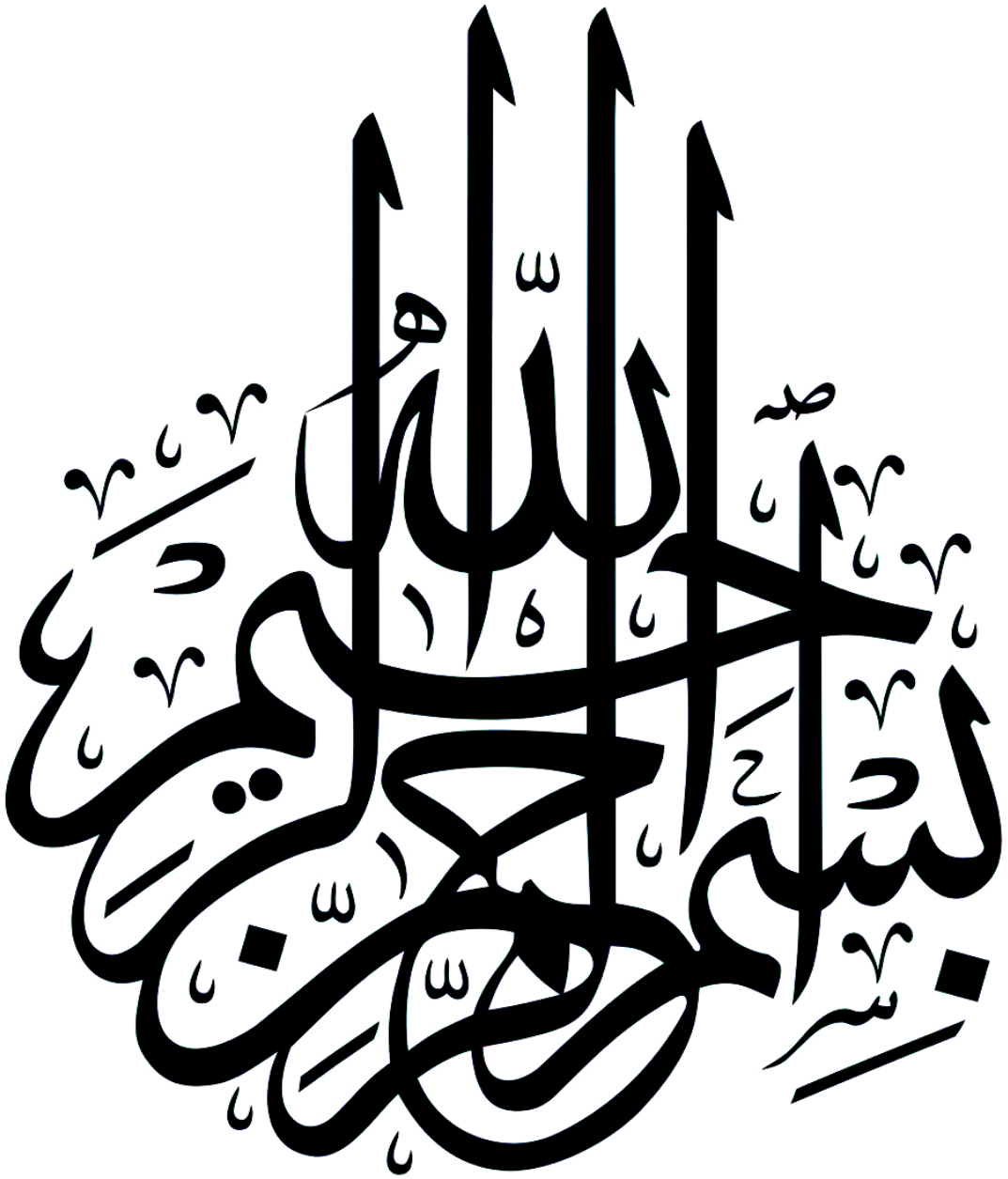
بسم الله الرحمن الرحيم

Acknowledgements

Praise be to God, who has guided and aided us. We would not have been able to complete this work without His guidance and grace. Now, we extend our sincere thanks and appreciation to everyone who contributed to the completion of this thesis. We also express our sincere gratitude to:

Dear Dr. Tinedert Imad Eddine, for the valuable advice, opinions, and information he provided us, which helped us prepare this research.

Our dear parents, who sacrificed their most precious possessions for our upbringing and education. We ask God to protect and care for them and all members of our esteemed family.

The distinguished professors from whom we learned, the professors of the Faculty of Science and Technology and the professors of the Electrical Engineering.

We would also like to thank all those who have helped us, directly or indirectly, and all. those who have served us. We have the utmost gratitude and respect for them.

Dedication

I dedicate this modest work to my dear parents, a source of life and happiness, for their support, patience, encouragement, and prayers during my university studies.

To my brothers and sisters, a source of joy and motivation.

To my entire family.

To everyone I have ever loved.

To my partner Khaoula.

Raoinak

Dedication

I dedicate this humble work

To my dearest parents,

Source of life's happiness, for their support,

Their patience, their encouragement, and their concern

My prayers during my university career.

To my dear brother and sister.

To all my loved ones.

Nabila

ملخص

في البداية، شهدت خلايا بيروفسكايت الشمسية المعتمدة على الرصاص اهتمامًا واسعًا في مجتمع الباحثين في البيروفسكايت، ولكن بسبب سُميّتها، أصبح من الضروري التوجّه نحو تطوير خلايا بيروفسكايت خالية من الرصاص. في هذه الدراسة، تم تحليل أداء الخلايا الشمسية الخالية من الرصاص باستخدام المحاكاة الرقمية من خلال برنامج SCAPS-1D. في المرحلة الأولى، تمت دراسة خلية شمسية مرجعية تعتمد على بنية ($FTO/SnS_2/RbSnI_3/Au$)، وقد أظهرت محاكاتها كفاءة تصل إلى 26.50%، متوافقة مع النتائج الرقمية المنشورة في الأدبيات. لزيادة الكفاءة، تم اقتراح إضافة طبقة امتصاص علوية من مادة $RbSnBr_3$، لتوسيع نطاق الامتصاص، وتكوين خلية ثنائية الطبقة ($FTO/SnS_2/RbSnBr_3/RbSnI_3/Au$)، مما أدى إلى تحسين الكفاءة لتبلغ 28.21%. في المرحلة الثانية، تم تقييم عدة مواد كطبقة ناقلة للإلكترونات (ETL) وتم اختيار مادة كبريتيد الكادميوم (CdS) نظراً لأدائها الأفضل. كما تم تحسين معلمات التصميم الأساسية مثل سمك الطبقات وتركيزات التطعيم، بالإضافة إلى دراسة تأثير دالة الشغل لمواد التلامس الخلفي من المعادن المختلفة. وأظهرت النتائج أن أفضل أداء تم تحقيقه عند سمك 500 نانومتر و1000 نانومتر لكل من طبقتي $RbSnI_3$ و$RbSnBr_3$، مع تركيزات تطعيم بمقدار 1×10^{18} سم$^{-3}$، مما أدى إلى كفاءة وصلت إلى 31.40%، وجهد دائرة مفتوحة 1.03 فولت، وكثافة تيار دائرة قصيرة 27.59 م.أ/سم^2، ومعامل التعبئة 85.83%، تحت إشعاع AM1.5G ودرجة حرارة 300 كلفن.

الكلمات المفتاحية: بيروفسكايت خالي من الرصاص، ممتص ثنائي الطبقة، الخلايا الشمسية، الكفاءة، التحسين، Scaps-1D.

Abstract

Initially, lead-based perovskite solar cells attracted significant attention in the perovskite research community. However, due to their toxicity, the transition toward lead-free perovskite materials became essential .This study focuses on optimizing the performance of lead-free perovskite solar cells using numerical simulations with the SCAPS-1D program. In the first phase, a reference solar cell with the structure (FTO/SnS_2/$RbSnI_3$/Au) was modeled, achieving a simulated efficiency of 26.50%, consistent with published numerical results .To enhance this performance, a new top absorber layer, $RbSnBr_3$, was introduced to extend the absorption spectrum, forming a bilayer structure (FTO/SnS_2/$RbSnBr_3$/$RbSnI_3$/Au), which raised the efficiency to 28.21%. In the second phase, various electron transport layers (ETLs) were evaluated, with cadmium sulfide (CdS) selected as the optimal material due to its superior performance .Key design parameters, including layer thickness and doping concentrations, were optimized. Furthermore, the effect of different back contact metals and their work functions on device performance was investigated. The best results were achieved with an $RbSnBr_3$ thickness of 1000 nm and $RbSnI_3$ thickness of 500 nm, both with doping concentrations of 1×10^{18} cm^{-3}. Under AM1.5G solar illumination and an operating temperature of 300 K, the optimized bilayer cell reached an efficiency of 31.40%, with a short-circuit current density of 27.59 mA/cm^2, open-circuit voltage of 1.03 V, and fill factor of 85.83%.

Keywords: Lead-free perovskite, bilayer absorber, solar cells, efficiency, optimization, Scaps-1D.

Table of contents

List of figures

List of tables

List of abbreviations

CB	Conduction Band
VB	Valence Band
E_F	Fermi energy
EHP	Electron hole pair
$RbSnI_3$	Rubidium Tin Iodide
$RbSnBr_3$	Rubidium Tin Bromide
SnS_2	Tin disulfide
CdS	Cadmium Sulfide
PSCs	Perovskite solar cells
FTO	fluorine-doped tin oxide
TCO	Transparent conduction oxide
ETL	Electron transport layer
SCAPS	Solar Cell Capacitance Simulator
R_s	Series resistance
R_{sh}	Shunt resistance
t_m	Thickness
E_g	Band gap energy
PCE	Performance Conversion efficiency
FF	Fill factor
J_{sc}	Short-circuit current density
V_{oc}	Open-circuit voltage
AM1.5G	Air Mass 1.5 Global
EQE	External quantum efficiency
χ_e	Electron affinity
μ_n	Electron mobility
μ_p	Hole mobility
N_v	Valence band effective density of states
N_c	Conduction band effective density of states
N_D	Donor Carrier concentration
N_A	Acceptor Carrier concentration
N_t	Defect Density

General Introduction

General Introduction

Solar cells are essential devices for converting solar energy into electrical energy and represent one of the most prominent renewable energy applications in the modern era. The discovery of solar cells dates back to the 19th century, when French physicist Alexandre Edmond Becquerel observed that directing sunlight onto electrical cells generates an electric current. Since then, solar cell technology has undergone continuous development. Solar cells vary in type depending on the materials used to manufacture them, including crystalline silicon cells, composite cells, organic cells, and perovskite-based cells. The operating principle of solar cells is based on the photovoltaic effect, whereby light energy is converted into electrical energy when the absorption of photons generates pairs of electrons and holes. Among the various types, perovskite solar cells (PSCs) have emerged as an innovative and rapidly developing technology in the field of photovoltaic energy conversion. Named after the perovskite materials that form the light-absorbing layer, these cells have attracted significant interest due to their excellent light absorption capabilities and low-cost production potential. These hybrid organic-inorganic compounds offer high power conversion efficiencies, making them promising alternatives to conventional silicon-based solar cells. Solar cell performance is typically evaluated using several key parameters, including open-circuit voltage (V_{oc}), short-circuit current (I_{sc}), fill factor (FF), and power conversion efficiency (PCE). Recent studies have reported significant improvements in solar cell performance, with perovskite solar cells achieving efficiencies of up to 26%, indicating significant progress in this field. However, the efficiency of single-junction solar cells is still limited by the Shockley-Queisser limit and thermodynamic constraints. One of the most effective strategies to overcome this limit is the use of double- or multi-layer heterojunction structures, where materials with different bandgaps are stacked to enable broader spectral absorption. In this context, the present thesis initially focuses on the modeling and analysis of a single-absorber perovskite solar cell (PSC) configuration. Building upon this reference structure, we propose a bilayer architecture by introducing $RbSnBr_3$ as an additional top absorber layer. This modification aims to enhance light absorption across a broader spectral range, resulting in the structure: FTO/SnS_2/$RbSnBr_3$/$RbSnI_3$/Spiro/Au. Drawing upon numerical data from previous studies, we evaluate and compare the performance of a single-absorber and bilayer PSC—comprising an $RbSnBr_3$ front absorber and an $RbSnI_3$ back absorber—using SCAPS-1D simulations. The study emphasizes the impact of the bilayer configuration on

improving the overall power conversion efficiency. In the second phase of this research, we aim to further enhance the efficiency of the $RbSnBr_3/RbSnI_3$ bilayer device by investigating various electron transport layers (ETLs) compatible with this structure. We also perform a systematic optimization of key design parameters, including the thickness and doping concentration of each layer, and evaluate the influence of different back contact metals. Ultimately, these efforts lead to the identification of an optimized, lead-free, bilayer perovskite solar cell design.

This thesis is organized into three chapters as follows:

Chapter 1:

This chapter provides a comprehensive overview of the principles underlying solar energy conversion, covering topics such as solar irradiation characteristics, the photovoltaic effect, semiconductor physics, and the behavior of p-n junctions. It further delves into the core operating mechanisms of solar cells, examining their performance metrics and the various loss mechanisms that limit efficiency. The chapter concludes with a detailed survey of different solar cell technologies, highlighting recent advancements and state-of-the-art developments in the field .

Chapter 2:

This chapter delves into the specifics of perovskite solar cells, with a focus on the chemical compositions most commonly used in their fabrication. Special attention is given to the materials used in this study, including transparent conductors such as FTO, ETLs like SnS_3 and CdS, and absorber layers such as $RbSnBr_3$ and $RbSnI_3$. The SCAPS-1D simulation tool is also explained in detail, highlighting essential commands and the key physical equations governing device simulation.

Chapter 3:

Titled Analysis and Interpretation of Numerical Simulation Results, this chapter begins by analyzing a simulated single-junction model and comparing it with the numerically developed bilayer structure. This chapter also presents a thorough optimization of critical design parameters and evaluates different ETLs materials to identify the most effective combination for high-efficiency, lead-free bilayer PSCs.

Chapter 01: Fundamentals of Solar Cells

1.1.Introduction

A solar cell is a core technology that converts solar energy into electrical energy, and is one of the most significant developments in the field of renewable energy. The roots of these cells date back to the 19th century, when French physicist Alexandre Edmond Becquerel observed that exposing electrical cells to sunlight generates an electrical current. Since Becquerel's pioneering discovery, solar cell technology has seen continuous development and numerous innovations. Today, there are different types of solar cells, distinguished by the materials used in their manufacture. These types include silicon core cells, composite solar cells, organic solar cells, and modern perovskite solar cells. The basic operation of a solar cell is based on the photocurrent effect, where the absorption of photons generates an electron gap and an electron hole, which converts light energy into electrical energy. Key metrics of solar cell performance include open-circuit voltage (V_{oc}), short-circuit current (I_{sc}), maximum power point (P_m), fill factor (FF), and overall efficiency (η). As solar cell technology advances, it holds great promise to play a crucial role in the global transition to sustainable energy sources.

In this chapter, we introduce the basic concepts of the p-n junction and the photovoltaic effect, which form the basis of most photovoltaic devices. These fundamentals are essential for understanding how solar cells work and convert sunlight into electricity. We then present the equivalent circuit diagrams of solar cells, and discuss the basic characteristics of their performance and methods for calculating them. In addition, we investigate the loss mechanisms in solar cells. Finally, we review the different types of solar cells and highlight the highest conversion efficiencies reported to date.

1.2.Solar radiation

Solar radiation refers to the energy emitted by the Sun in the form of electromagnetic waves, including visible light, ultraviolet (UV) radiation, and infrared (IR) radiation. This energy is the primary source of heat and light on Earth, supporting life and driving various natural processes. Solar radiation is measured in watts per square meter (W/m^2) and varies depending on factors such as the time of day, geographic location, and weather conditions. It plays a crucial role in renewable energy technologies, particularly in solar power generation, where solar panels capture this radiation and convert it into electricity [1].

1.2.1. Air Mass

The electromagnetic radiation emitted by the Sun outside the Earth's atmosphere is referred to as AM 0 (Air Mass 0). On the other hand, AM 1 represents the sunlight that has passed through Earth's atmosphere, as shown in Figure 1.1. According to Planck's Law of Radiation, AM 0 represents the radiation emitted by a black body, which corresponds to the Sun's surface at a temperature of 5778 K, as illustrated in Figure 1.1. The path the radiation takes through the atmosphere ($1/\cos\theta$), along with various natural factors (Figure 1.1), alters the light, creating the AM x spectrum, as shown in Figure 1.2, where x = 1, 2, 3, or 4. The area under the AM 1.5 curve, corresponding to ($1/\cos 48°$), results in an irradiance of 1000 W/m² [10]. Therefore, AM 1.5 solar radiation is used as a standard for evaluating the actual performance of solar cells, as it represents the optimal conditions for sunlight to reach the Earth's surface when it enters the atmosphere vertically [2].

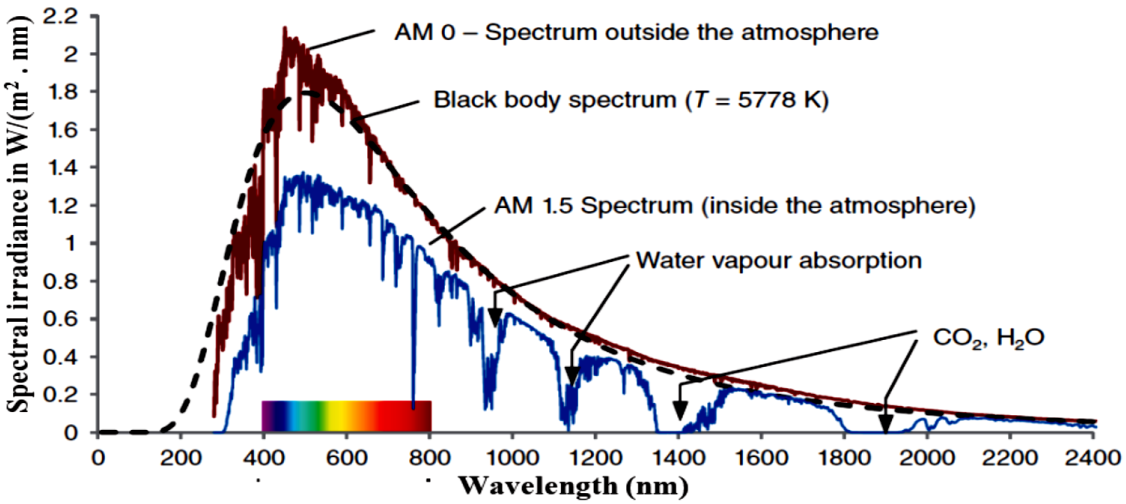

Figure 1.1: *Solar spectrum beyond and within the Earth's atmosphere.*

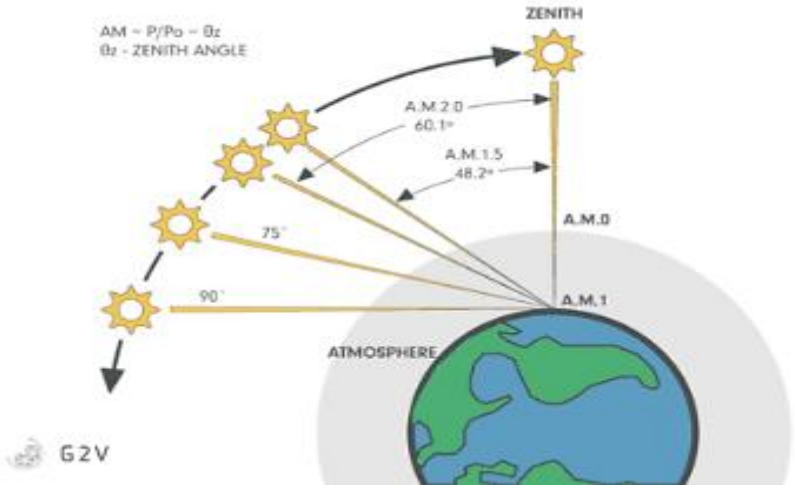

Figure 1.2: *Air Mass Spectrum Overview [3].*

The impact of AM1.5 solar radiation on solar cells can be summarized in three key points:

1. **Performance Evaluation:** AM1.5 radiation provides a standardized benchmark to assess the performance of solar cells, making it easier to compare different technologies and materials.
2. **Design Optimization:** Understanding how a solar cell performs under AM1.5 conditions enables improvements in design, enhancing its ability to absorb solar energy efficiently.
3. **Enhancing Manufacturing Processes:** Performance data based on AM1.5 radiation can guide adjustments in manufacturing processes to improve the quality of solar cells. This makes AM1.5 an essential tool for driving innovation and advancement in the solar energy sector.

1.3.Solar cells

1.3.1. The concept of solar cells

A solar cell, also known as a photovoltaic (PV) cell, is a semiconductor device that directly converts sunlight into electrical energy through the photovoltaic effect. This process occurs when light photons are absorbed by the material of the solar cell, which then excites electrons and creates an electric current.

The basic structure of a solar cell consists of a layer of semiconductor material, typically silicon, which is treated or "doped" with impurities to create two types of semiconductors: p-type (positive) and n-type (negative). When these two materials are placed together, they form a p-n junction, which is the key to generating electricity. The interaction between these layers creates an electric field at the junction, which helps to separate the electron-hole pairs created by the absorption of light, causing the electrons to flow toward the negative side and the holes to move toward the positive side. This flow of electrons generates an electric current, which can be harnessed for external use.

1.3.2. History of Solar Cells

The concept of solar cells was first experimentally demonstrated by French physicist Edmond Becquerel in 1839. At just 19 years old, Becquerel created the world's first photovoltaic cell in his father's laboratory. In 1873, Willoughby Smith described the "Effect of Light on Selenium during the Passage of an Electric Current" in a paper published in Nature. This marked another key step in understanding solar energy. In 1883, Charles Fritts created the first solid-state photovoltaic cell by coating selenium with a thin layer of gold, forming junctions; however, its efficiency was only about 1% [4].

Other significant milestones in the history of solar cells include:

- 1888Alesandr Stoletov, a Russian physicist, built the first cell based on the outer photoelectric effect, which had been discovered by Heinrich Hertz in 1887 [5].
- 1904 Julius Elster and Hans Friedrich Geitel developed the first practical photoelectric cell [6].
- 1905Albert Einstein introduced a new quantum theory of light, explaining the photoelectric effect in a groundbreaking paper that earned him the Nobel Prize in Physics in 1921[7].
- 1941Vadim Lashkaryov discovered the p-n junctions in Cu_2O and Ag_2S protocells, which was an important step towards modern solar cell technology [8] .
- 1946Russell Ohl patented the modern junction semiconductor solar cell, contributing to advances that would later lead to the invention of the transistor [9].
- 1948In the journal Physical Review, Kurt Lehovec may have been the first to explain the photovoltaic effect in a peer-reviewed publication[10].
- 1954 The first practical photovoltaic cell was publicly demonstrated at Bell Laboratories.[11] The inventors were Calvin Souther Fuller, Daryl Chapin and Gerald Pearson [12].
- 1958 lar cells gained widespread recognition when they were used on the Vanguard I satellite [13].

These key achievements highlight the gradual evolution of solar cell technology, tracing its journey from initial concepts to solar energy solutions.

1.3.3. Photovoltaic Effect

The photovoltaic effect is a process in which a material generates an electric current or voltage when exposed to light. This phenomenon is the basis for how solar panels work, allowing the cells within the panel to convert sunlight into electrical energy. The effect was first discovered in 1839 by French physicist Edmond Becquerel. While conducting experiments with wet cells, he observed that the voltage of the cell increased when its silver plates were exposed to sunlight. This discovery laid the foundation for the development of solar energy technology, as it demonstrated that light could directly generate electricity [14].

1.3.4. Working principle of solar cell

The photovoltaic effect is the core principle behind the operation of solar cells. Solar cells are made from two different types of semiconductors—p-type and n-type—that are joined together to form a p-n junction. The interaction between these two types of semiconductors creates an electric field at the junction, which drives the movement of electrons toward the positive p-side and holes toward the negative n-side. This electric field ensures that negatively charged particles (electrons) and positively charged particles (holes) move in opposite directions [14].

Light, which consists of photons (tiny packets of electromagnetic energy), can be absorbed by the photovoltaic material [15]. When light with an appropriate wavelength strikes the solar cell, the energy from the photon is transferred to the semiconductor atoms within the p-n junction. Specifically, this energy is absorbed by the electrons, causing them to be excited and jump to a higher energy state known as the conduction band. This jump leaves behind a "hole" in the valence band, where the electron was initially located. The movement of the electron due to this added energy creates two charge carriers: an electron-hole pairs [14].

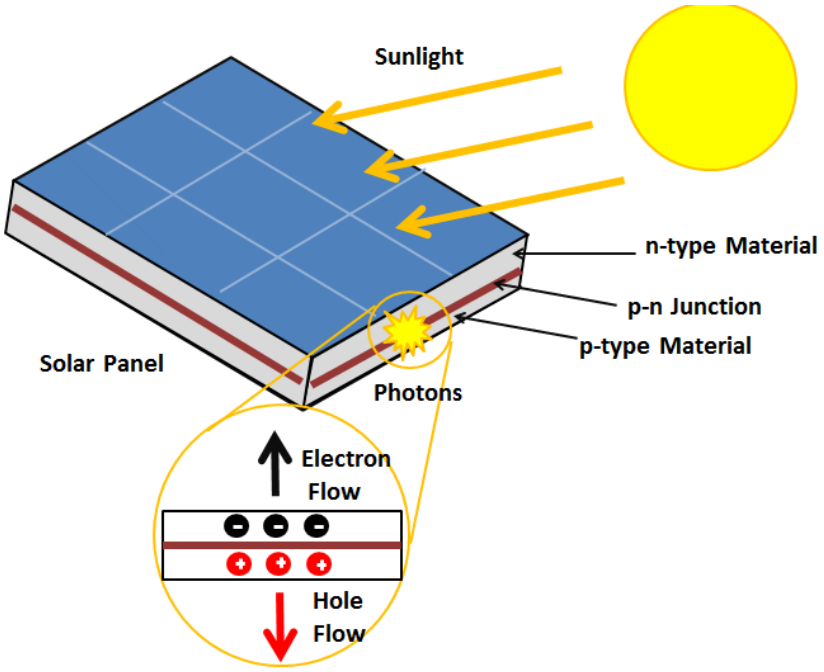

Figure 1.3: *Photovoltaic effect [16].*

When electrons are in their unexcited state, they are bound to atoms within the semiconductor material, forming bonds that prevent them from moving. However, when they gain energy and move to the conduction band, they become free to travel through the material. The electric field created by the p-n junction causes the electrons and holes to move in opposite directions. Instead of being drawn to the p-side, the excited electron typically moves toward the n-side. This

movement of the electron generates an electric current within the solar cell. As the electron moves, it leaves behind a "hole" in the p-type material, which can also move, but in the opposite direction, toward the p-side. This process, where both the electron and the hole move in different directions, creates the flow of current in the solar cell. A diagram illustrating this process can be seen in Figure 1.3.

1.3.5. P-N junction under illumination

When a p-n junction semiconductor is exposed to light, it generates more electron-hole pairs. This increase in charge carrier concentration causes minority carriers (holes in the n-type region and electrons in the p-type region) to flow across the depletion region into the quasi-neutral regions. Electrons move from the p-type region to the n-type region, and holes move from the n-type region to the p-type region. This movement creates a photocurrent density (J_{ph}), which adds to the current from thermal generation (J_{gen}). In the absence of an external connection between the p-type and n-type regions, the junction remains in an open-circuit condition. As a result, the reverse recombination current balances the current from thermally and photo-generated carriers. This decreases the electrostatic potential barrier across the depletion region, which in turn increases the recombination current [17].

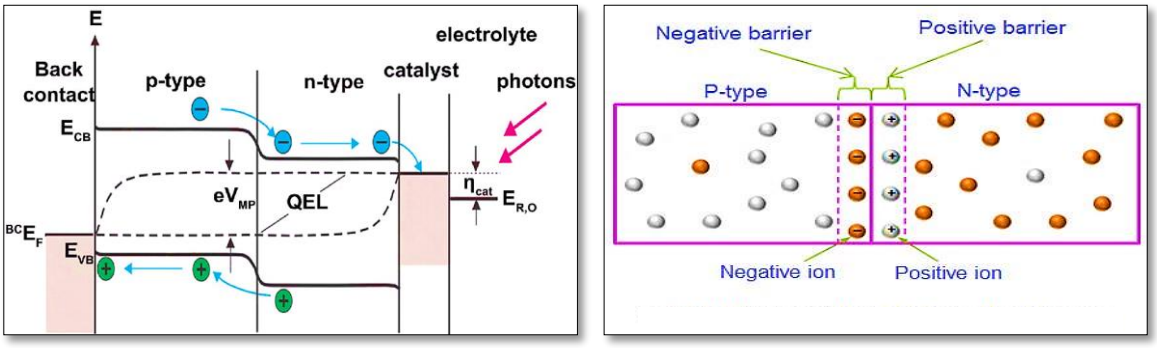

Figure 1.4: *P-N junction under illumination.*

1.3.6. Properties of photovoltaic cells

The performance parameters of a solar cell include the *open-circuit voltage*, *short-circuit current*, *fill factor*, and the *photoelectric conversion efficiency*.

1.3.6.1. Maximum power point (Pm)

The Maximum Power Point (P_m) in solar cells is the point where the highest power generation is achieved. It is determined by monitoring the electrical current and voltage output of the cell to identify the point that provides maximum efficiency. This point depends on several factors, including temperature, light intensity, and biometric parameters. DC-DC converters are used to

regulate the voltage and current for optimal performance. The term "Maximum Power Point Tracking (MPPT)" refers to techniques used to precisely identify this point, enabling the most efficient utilization of available solar energy [18].

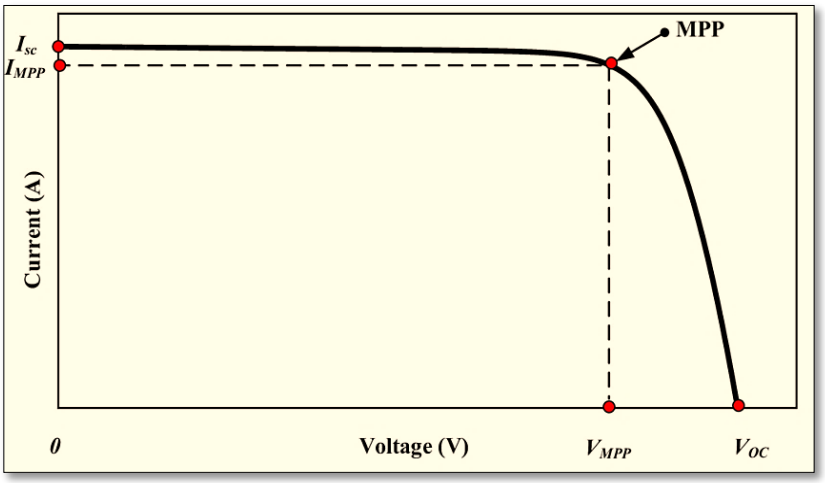

***Figure 1.5**: curve for Maximum power point (Pm).*

1.3.6.2. Short circuit current (I_{sc})

The short-circuit current (I_{sc}) is the maximum current a solar cell or panel can produce when its terminals are directly connected (short-circuited). This is a critical parameter for assessing the efficiency of a solar cell. Short-circuit current is typically measured under standard test conditions to ensure accurate comparisons between different types of solar cells [18]. When comparing solar cells made from the same material, the most important material factors are diffusion length and surface passivation. In cells with perfectly passivated surfaces and uniform energy generation, the equation for short-circuit current density can be approximated to reflect the cell's efficiency [19]**:**

$$J_{SC} = qG(L_n + L_p) \tag{1.1}$$

Where:

- G is the generation rate.
- L_n is the electron diffusion length.
- L_p is the hole diffusion length.

The short circuit current, I_{SC}, is the short circuit current density, J_{SC}, times the cell area:

$$I_{SC} = J_{SC} * A \tag{1.2}$$

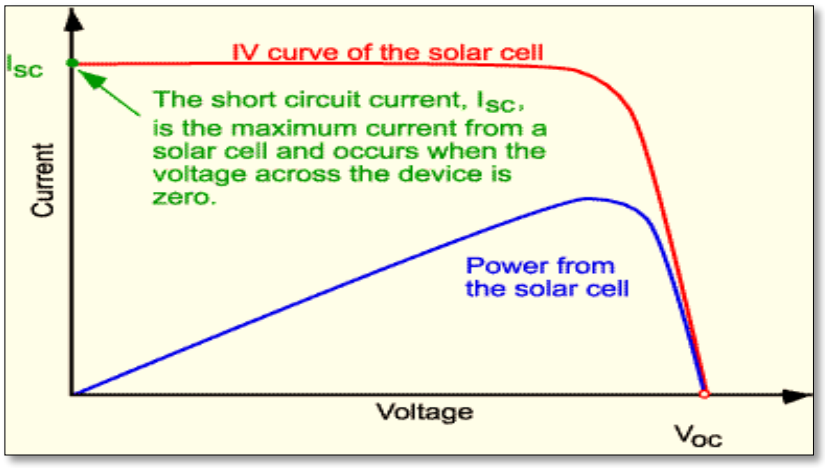

Figure 1.6: *curve for Short circuit current (I_{sc}).*

1.3.6.3. Open circuit voltage (V_{oc})

Open circuit voltage (V_{oc}) is the maximum voltage that a solar cell, battery, or any other electrical device can produce when there is no load connected to it. It is a measure of the potential difference across the terminals of the device in an open circuit condition [19].

An equation for V_{oc} is found by setting the net current equal to zero in the solar cell equation to give**:**

$$V_{oc} = \frac{nkT}{q} ln\left(\frac{I_L}{I_0} + 1\right) \tag{1.3}$$

The V_{oc} can also be determined from the carrier concentration:

$$V_{oc} = \frac{kT}{q} ln\left[\frac{(N_A+\Delta n)\Delta n}{n_i^2}\right] \tag{1.4}$$

Where the dark saturation current (I_0), the light-generated current (I_L), the ideality factor (n), the temperature (T), the doping concentration (N_a), the excess carrier concentration (Δn), and the intrinsic carrier concentration (n_i).

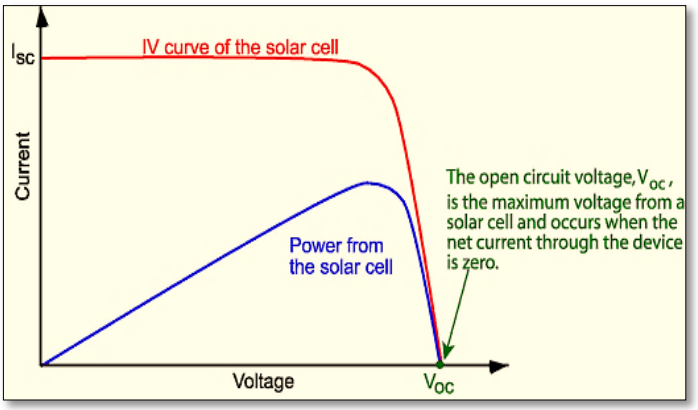

Figure 1.7: *curve for Open circuit voltage.*

1.3.6.4. Fill Factor (FF) Ratio

The fill factor (FF) is a measure used to assess the efficiency of solar cells and other electrical devices, indicating the proportion of electrical power generated relative to the maximum possible power that can be extracted. It is calculated by dividing the maximum electrical output achievable under ideal conditions by the ratio of the actual electrical power produced by the device to the power extracted from it [19]. The formula for the FF is:

$$FF = \frac{V_{MP}\, I_{MP}}{V_{OC}\, I_{SC}} \tag{1.5}$$

Where:

- Open-circuit voltage, V_{oc}.
- Short-circuit current, I_{sc}.
- Voltage at max power, V_{MP}.
- Current at max power, I_{MP}.

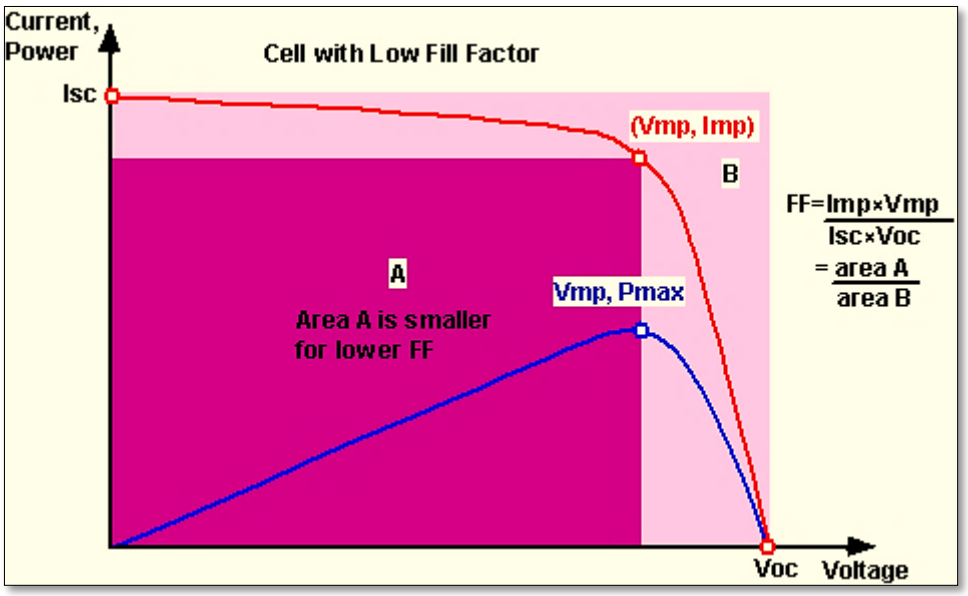

Figure 1.8: *curve for Fill Factor (FF).*

1.3.6.5. Efficiency

The efficiency of a solar cell is a key metric for comparing the performance of different cells. It is defined as the ratio of the energy produced by the cell to the solar energy received. Efficiency depends on temperature, light intensity, and the solar spectrum, reflecting the cell's performance.

To measure efficiency accurately, tests are conducted under standard conditions, such as a temperature of 25°C and AM1.5 radiation.

$$\eta = \frac{V_{OC}\, I_{SC}\, FF}{P_{in}} \tag{1.6}$$

Where:

- V_{oc} is the open-circuit voltage.
- I_{sc} is the short-circuit current .
- FF is the fill factor .
- Input Power, P_{in} .

1.3.7. The equivalent circuit of a solar cells

The equivalent circuit of a solar cell typically consists of:

1. **Current Source (I_{ph}):** Represents the photocurrent generated when the solar cell is exposed to light.
2. **Diode (D):** Models the p-n junction, representing the behavior of the cell under dark conditions.
3. **Series Resistance (R_S):** Accounts for the resistance to current flow due to the materials and contacts in the cell.
4. **Shunt Resistance (R_{SH}):** Represents leakage current bypassing the diode, which can reduce the cell's efficiency.

This circuit model helps understand and analyze the I-V characteristics of the solar cell [20].

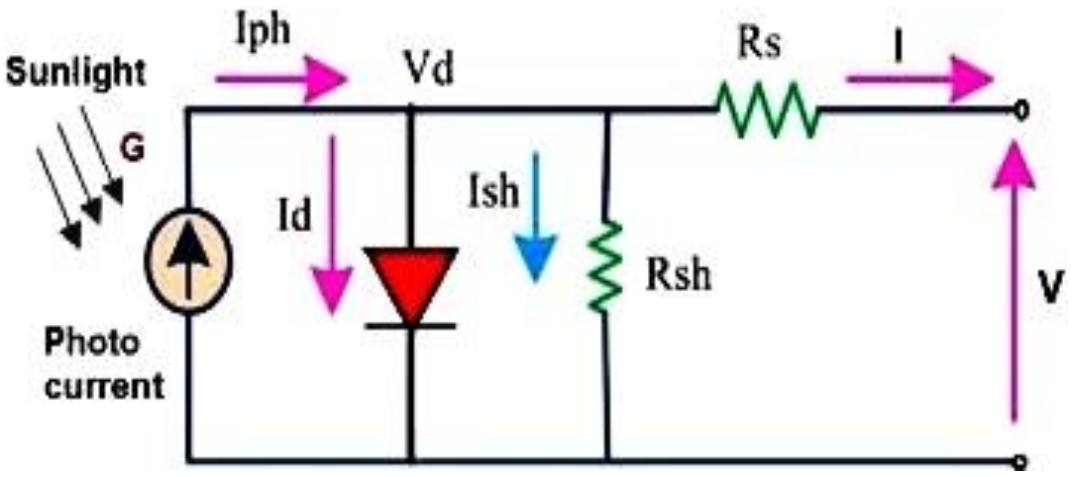

***Figure 1.9**: Schematic representation of a solar cell's equivalent circuit.*

Parallel to this ideal current generator is a diode. The power that can be extracted from a device (P) is equal to current (I) multiplied by voltage (V):

$$P = V \times I \tag{1.7}$$

Equations describing and simulating solar cells can be derived from this ideal circuit design. This helps define important parameters used to characterize solar cells. The current through the load is defined as the total current generated minus the current passing through the diodes and the current lost due to shunt resistance.

$$I = I_{Gen} - I_{Diode} - I_{sh} \tag{1.8}$$

where I is current extracted, I_{Gen} is the generated current, I_{Diode} is diode current, and I_{sh} is current lost to shunt resistance. This equation gives us the characteristic current-voltage graph shape we see for solar cells.

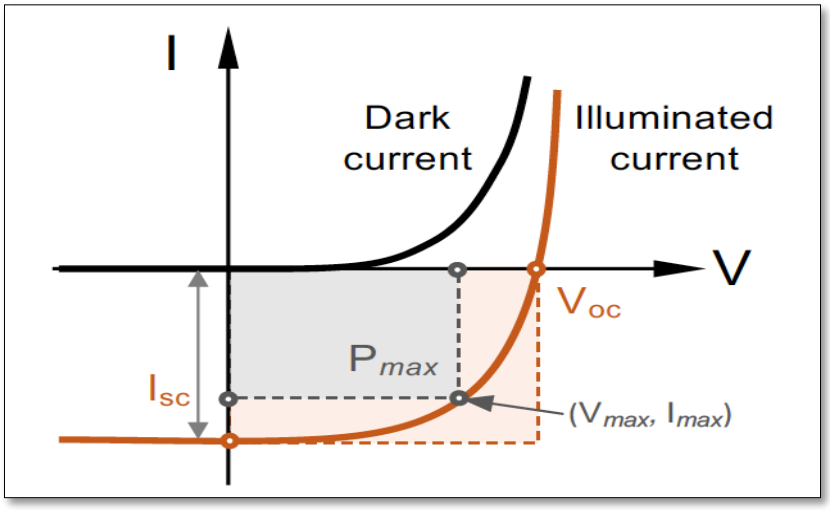

Figure 1.10: *The dark and illuminated I-V characteristics of the solar cell.*

1.3.8. Quantum efficiency

Quantum Efficiency measures a solar cell's ability to convert light into electricity when exposed to radiation. It is defined as the ratio of the number of electrons generated in the cell to the number of photons absorbed by the cell. In simple terms, it shows how effectively the cell transforms incoming light particles (photons) into electrical current.

1.3.8.1. External Quantum Efficiency EQE

EQE, or External Quantum Efficiency, is the ratio of the number of charge carriers collected by the solar cell to the number of incident photons of a given energy shining on the solar cell. This measurement accounts for the reflection losses of the solar cell [7]:

$$EQE(\lambda) = \frac{Number\ of\ collected\ electron{-}hole\ pairs}{Number\ of\ incident\ photons} = \frac{Isc}{P_{in}} \cdot \frac{hc}{q\lambda} \quad (1.9)$$

Where P_{in} is incident power, I_{sc} is Short circuit current, h is Planck constant (6.626×10^{-34} J.s), λ is wavelength of the incident photons, and c is speed of light (2.998×10^{8} m/s).

1.3.8.2. Internal Quantum Efficiency IQE

Internal Quantum Efficiency (IQE) is the ratio of the number of charge carriers collected by the solar cell to the number of photons of a specific energy that are absorbed by the cell. Unlike External Quantum Efficiency (EQE), IQE does not take into account the losses due to reflections. The formula for IQE is given by [7]:

$$IQE = \frac{Number\ of\ collected\ electron{-}hole\ pairs}{Number\ of\ absorber\ photons} = \frac{EQE}{1-R} \quad (1.10)$$

where R is the reflection coefficient from the top surface of solar cell.

1.3.9. Loss mechanisms in Solar Cells

Cell losses are a significant issue as they greatly reduce the efficiency of the cells. Some of these losses can be prevented, but certain losses are inherent to the system. These losses are generally categorized into two main types: electrical and optical. The majority of these losses are represented in the following figure.

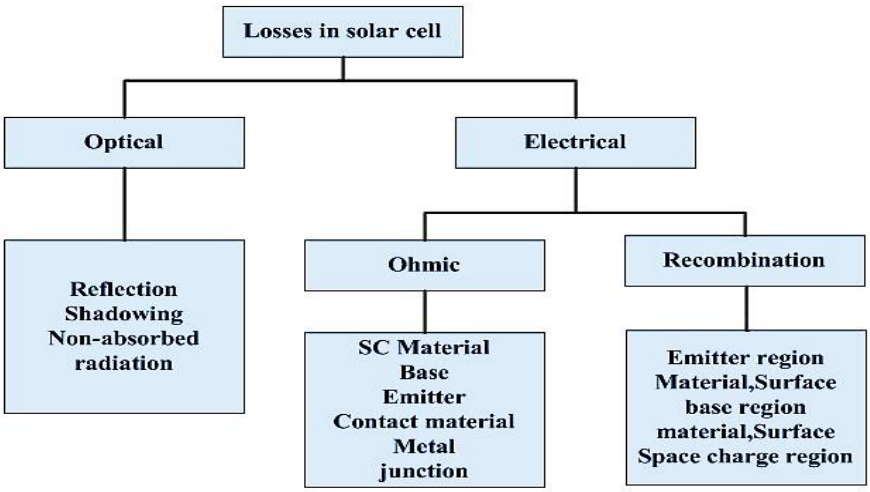

Figure 1.11: *Different losses in the solar cell.*

1.3.9.1. Optical losses in the solar cell

Optical losses in solar cells occur when light is not effectively absorbed or utilized. These include:

Reflection Losses: Some light is reflected off the cell's surface instead of being absorbed.

Transmission Losses: Light passes through the cell without being absorbed.

Sub-bandgap Absorption: Photons with energy lower than the material's bandgap cannot be absorbed.

Spectral Mismatch: Photons with energy higher than the bandgap lose excess energy as heat, while those with lower energy are not absorbed [21].

1.3.9.2. Electrical losses in the solar cell

Electrical losses in solar cells mainly occur due to factors like limited conductivity of the doped semiconductor, which leads to ohmic losses. Although using narrow, elevated contact fingers can reduce losses at contact points, increasing the n-doping level improves performance but also raises recombination rates. Additionally, the Schottky contact between the semiconductor and metal creates a potential barrier that reduces the open circuit voltage [22].

1.3.10. Different Types of Solar Cells

Solar cells are presently categorized into four main generations based on the period of development and the types of materials used in their production. Figure 1.12 provides a summary of these different generations of solar cells.

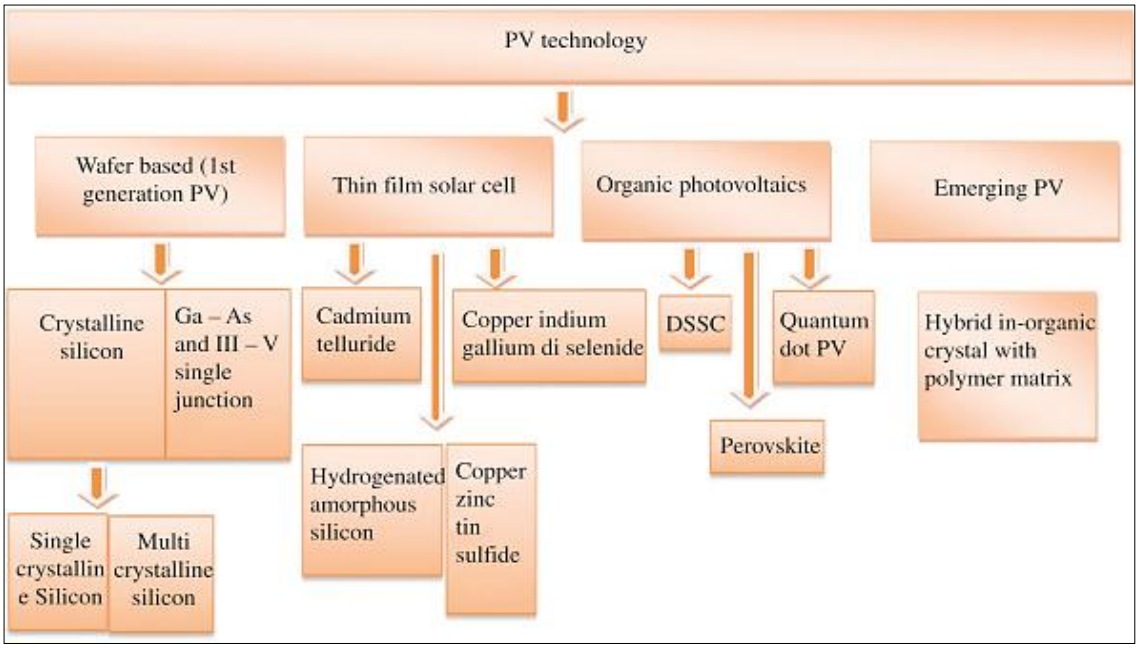

Figure 1.12: *Generations of solar cells.*

The *National Renewable Energy Laboratory (NREL)* tracks the highest confirmed conversion efficiencies of photovoltaic technologies since 1976 [23]. Currently, perovskite solar cells have achieved an efficiency of 26.7%, as depicted in Figure 1.13. showcasing their evolution and advancements in solar technology.

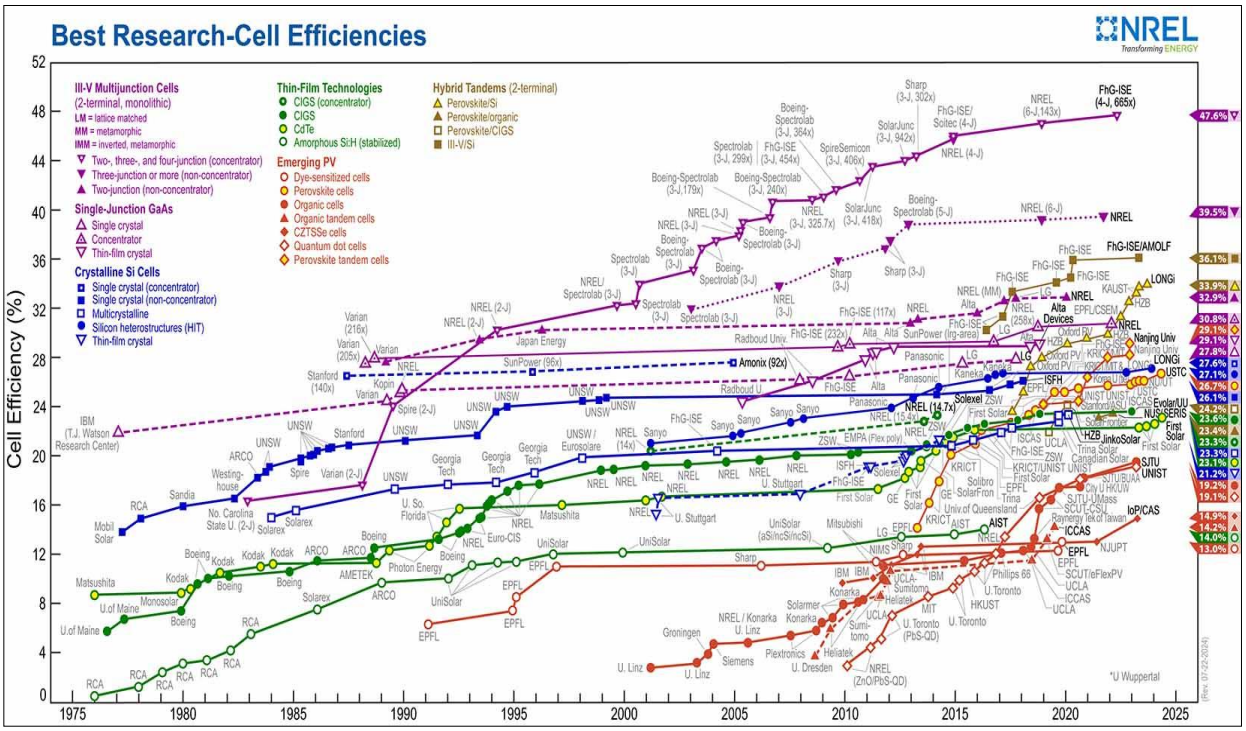

Figure 1.13: *Chart showing the highest research-cell efficiencies, adapted from [19].*

1.3.10.1. First generation: Silicon Solar Cells

The first generation of solar cells includes Mono-crystalline, Multi-crystalline silicon, and Gallium Arsenide (GaAs) cells. These are the oldest and most commonly used types due to their high efficiency, but they are expensive to produce. Since silicon is abundant in the Earth's crust, raw materials are expected to remain accessible in the future, potentially reducing costs [22].

a) Monocrystalline cells:

A monocrystalline silicon solar cell consists of a single, continuous silicon crystal structure, also known as monocrystalline solar cells (Mono-Si). Its uniform crystalline arrangement reduces barriers to electron flow, enhancing its efficiency in transforming solar energy into electricity. While these cells are typically more expensive to produce compared to polycrystalline cells, they deliver better performance and efficiency across diverse environmental conditions [24]. The maximum laboratory efficiency recorded for single-junction monocrystalline cells is 27.6% [23,21].

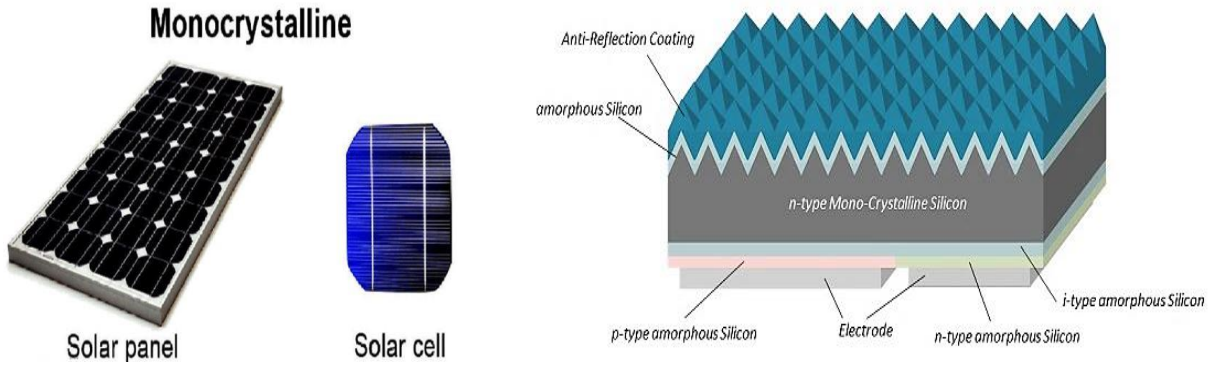

Figure 1.14: *Monocrystalline solar cells.*

b) MultiCrystalline Solar Cells

This type of solar cell is constructed from silicon wafers composed of many small crystals. In contrast to monocrystalline cells, polycrystalline cells feature multiple crystal grains, which makes their production process simpler and more cost-effective. However, their efficiency tends to be somewhat lower than that of monocrystalline cells due to the crystal boundaries that can hinder electron movement [25]. The maximum laboratory efficiency recorded for single-junction polycrystalline cells is 23.3% [23,21].

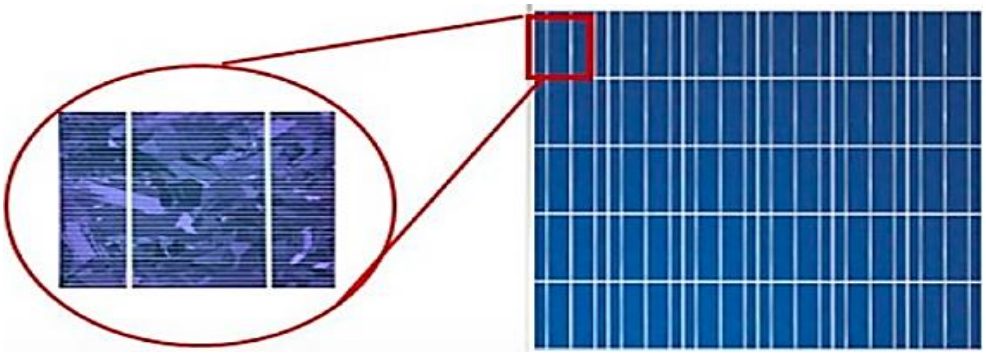

Figure 1.15: *Polycrystalline Solar Panel.*

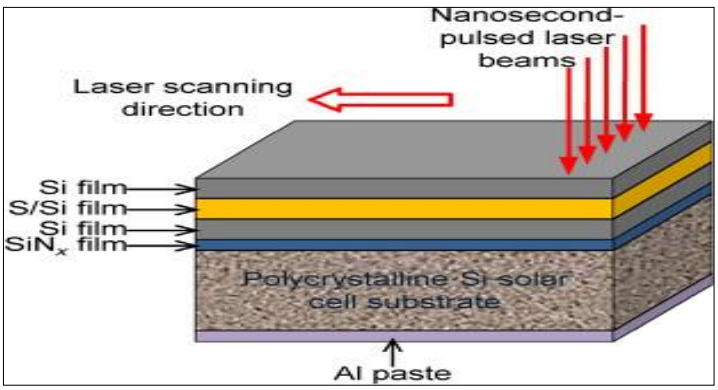

Figure 1.16: *A diagram showing the layers of a Polycrystalline Solar Cells.*

1.3.10.2. Thin film solar cells

Thin film solar cells, commonly referred to as second generation solar cells, are a kind of solar energy technology that converts light into electricity by using thin layers of semiconductor materials. Comparing these cells to conventional crystalline silicon solar cells reveals that they are lighter and thinner. These thin films are made from a variety of materials, including amorphous silicon (a-Si), copper indium gallium selenide (CIGS), and cadmium telluride (CdTe) [26]. In terms of performance, CdTe cells have achieved an efficiency of 23.1%, while CIGS cells have reached 23.6%. For a-Si cells, the efficiency is about 14% [23,21].

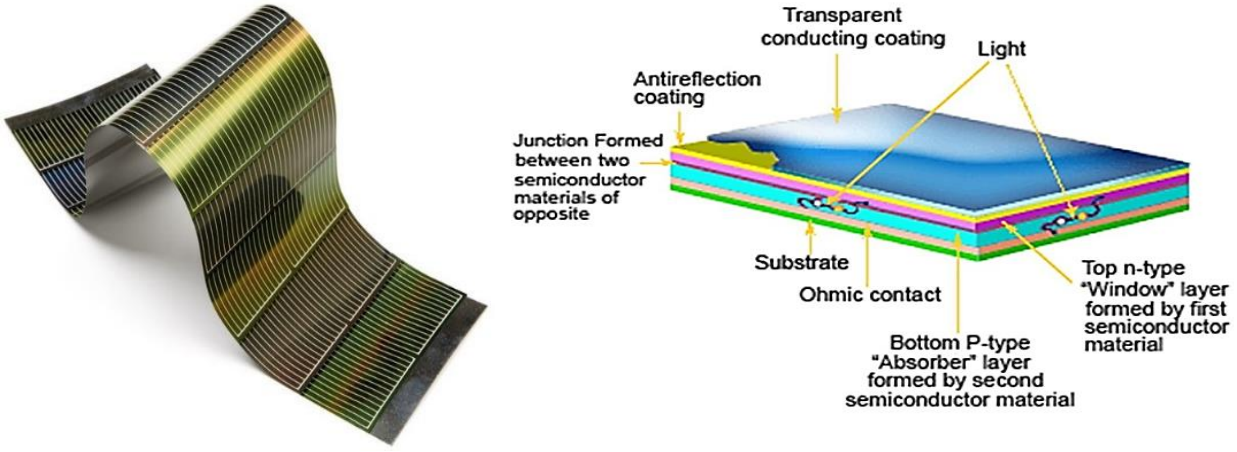

Figure 1.17: *Thin film solar cells.*

1.3.10.3. Emerging Photovoltaic Technologies of the Third Generation

Third-generation solar cells, like their second-generation counterparts, utilize thin-film technology but remain in the research and development phase. Ongoing studies focus on fabricating these advanced thin-film cells using a variety of organic and inorganic materials, notably perovskite compounds. These next-generation cells aim to achieve high power conversion efficiency (PCE) through advanced mechanisms such as multijunction tandem structures, multiple exciton generation (MEG), intermediate band (IB) formation, hot carrier extraction, and thermophotovoltaic processes [23]. Additionally, the discovery and integration of novel materials represent a central research direction. Among these, perovskite solar cells have reached an experimental efficiency of 26.7% to date [14,19].

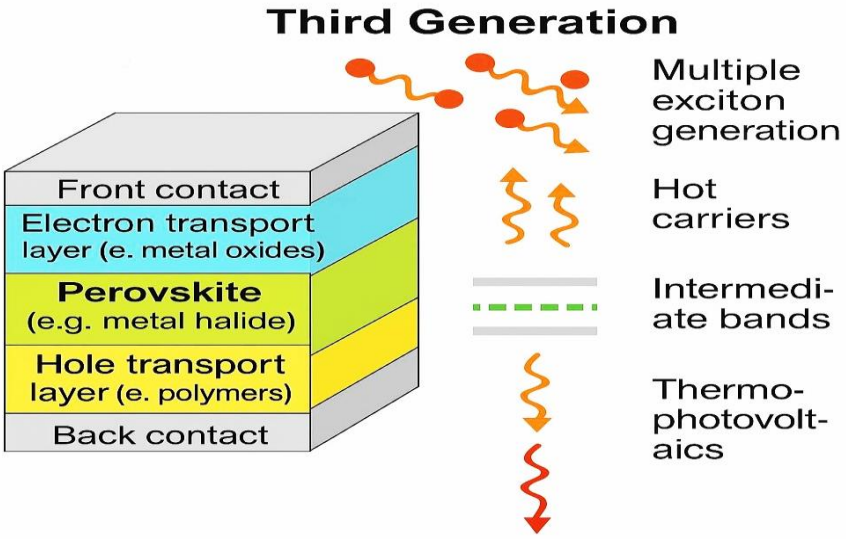

Figure 1.18: *General structure of perovskite solar cells.*

1.4.Conclusion

In this chapter, we have explored the fundamental principles that govern the operation of solar cells. Beginning with an overview of solar radiation and the concept of the Air Mass, we established the importance of sunlight as a key energy source for photovoltaic devices. We then delved into the essential physics of solar cells, including the photovoltaic effect and the role of the p-n junction under illumination, which enables the conversion of light into electrical energy.

A detailed examination of the working principle and performance parameters of solar cells was provided, including the I_{sc}, V_{oc}, FF, and overall efficiency. We also introduced the equivalent circuit model to better understand the electrical behavior of these devices and discussed quantum efficiency as a measure of how effectively a solar cell converts photons into charge carriers.

Additionally, we analyzed the key loss mechanisms—both optical and electrical—that limit solar cell performance, offering insight into challenges that must be addressed to enhance device efficiency. Finally, we reviewed the major types of solar cells across three generations, highlighting both established and emerging technologies, as well as their respective conversion efficiencies.

This foundational knowledge sets the stage for the more advanced discussions in subsequent chapters, where we will explore material innovations, device architectures, and simulation tools aimed at pushing the limits of photovoltaic performance.

References Chapter 1:

[1] Duffie, J. A., & Beckman, W. A. (1980). *Solar engineering of thermal processes* (p. 16591). New York: Wiley.

[2] Marzo, A., Ferrada, P., Beiza, F., Alonso-Montesinos, J., Ballestrín, J., & Román, R. (2016). Comparison of atacama desert solar spectra vs. ASTM G173-03 reference spectra for solar energy application. In *International Energy Society. Conference Proceedings*.

[3] Quaschning, V. (2014). *Understanding renewable energy systems*. Routledge.

[4] Marques Lameirinhas, R. A., Torres, J. P. N., & de Melo Cunha, J. P. (2022). A photovoltaic technology review: History, fundamentals and applications. *Energies*, *15*(5), 1823.

[5] Gevorkian, P. (2007). Sustainable energy systems engineering: the complete green building design resource. *(No Title)*.

[6] Julius (Johann Phillipp Ludwig) Elster: 1854 - 1920. Adventures in Cybersound. Archived from the original on 8 March 2011. Retrieved 15 October 2016.

[7] The Nobel Prize in Physics 1921: Albert Einstein, Nobel Prize official page.

[8] Lashkaryov, V. E. (1941). Investigations of a barrier layer by the thermoprobe method. *Izv. Akad. Nauk SSSR, Ser. Fiz*, *5*(4-5), 442-446.

[9] Light sensitive device U.S. patent 2,402,662 Issue date: June 1946.

[10] Lehovec, K. (1948). The photo-voltaic effect. *Physical Review*, *74*(4), 463.

[11] Lau, W. S. (2017). *ULSI Front-End Technology: Covering from the First Semiconductor Paper to CMOS FINFET Technology*. World Scientific.

[12] Chodos, A. (2009). April 25, 1954: Bell labs demonstrates the first practical silicon solar cell. *APS News-This month in Physics history*.

[13] Tsokos, K. A. (28 January 2010). *Physics for the IB Diploma Full Colour*. Cambridge University Press.

[14] G. Boyle. *Renewable Energy: Power for a Sustainable Future*, 2nd ed. Oxford, UK: Oxford University Press, 2004.

[15]Mr.Solar. (April 17, 2025). Photovoltaic Effect [Online]. Available: http://www.mrsolar.com/photovoltaic-effect/.

[16] Created internally by a member of the Energy Education team. Adapted from: Ecogreen Electrical. (August 14, 2015). *Solar PV Systems* [Online].

[17] Bajaj, N. S., & Joshi, R. A. (2021). Energy materials: synthesis and characterization techniques. In *Energy materials* (pp. 61-82). Elsevier.

[18] S.M. Sze, M.-K. Lee, *Semiconductor Devices: Physics and Technology: Physics and Technology*, Wiley Global Education, 2012.

[19] https://www.pveducation.org/pvcdrom/solar-cell-operation

[20] https://www.ossila.com/pages/history-of-solar-cells

[21] Green, M. A., Dunlop, E. D., Yoshita, M., Kopidakis, N., Bothe, K., Siefer, G., ... & Hao, X. (2024). Solar cell efficiency tables (Version 64).

[22] Luceño-Sánchez, J. A., Díez-Pascual, A. M., & Peña Capilla, R. (2019). Materials for photovoltaics: State of art and recent developments. *International journal of molecular sciences*, *20*(4), 976.

[23] Best research-cell efficiencies chart. NREL, (n.d.). https://www.nrel.gov/pv/cell-efficiency.html (accessed august 08, 2024).

[24] Fraas, L. M., & O'Neill, M. J. (2014). *Low-cost solar electric power* (pp. 1-12). New York: Springer.

[25] Green, M. A. (1982). Solar cells: operating principles, technology, and system applications. *Englewood Cliffs*.

[26] Chopra, K. L., Paulson, P. D., & Dutta, V. (2004). Thin-film solar cells: an overview. *Progress in Photovoltaics: Research and applications*, *12*(2-3), 69-92.

Chapter 02: Perovskite Solar Cells and the SCAPS Simulation Tool

2.1. Introduction

The perovskite layer is a key component in composite solar cells, performing a vital function in converting sunlight into electrical energy. Perovskite materials exhibit exceptional properties that make them highly efficient at absorbing light and facilitating charge transport. These materials typically consist of metal-organic compounds with a three-dimensional crystal structure—the lead-free halide perovskite $RbSnM_3$ (M = I, Br, Cl)—and exhibit excellent light absorption across the solar spectrum, enabling them to achieve impressive power conversion efficiencies. Furthermore, the superconductivity of the perovskite layer enhances the mobility of electrons and holes within the solar cell. The study and innovation of perovskite layers remain an active and promising field in renewable energy, as their incorporation into composite solar cells marks a significant step toward improving the efficiency of converting solar energy into electricity [1].

In this chapter, we will define perovskite materials, with an emphasis on those used in our simulations, including $RbSnBr_3$, SnS_2, CdS and $RbSnI_3$. Additionally, we will introduce the simulation tool SCAPS-1D, discussing its features and detailing the methodology for conducting solar cell simulations. This will equip readers with a thorough understanding of the software and its application in our study.

2.2. Perovskite cell

The term "perovskite" does not refer to a single material like silicon or cadmium telluride but rather represents a broad class of compounds. These materials are collectively known as "perovskites," a name derived from the mineral discovered in 1839 and named in honor of Russian mineralogist L.A. Perovski. The original perovskite mineral, calcium titanium oxide ($CaTiO_3$), is characterized by its unique crystal structure, which is composed of three main components: A, B, and X [2].

Perovskite layers are highly attractive for application in solar cells due to several advantages, including:

- ✓ **High light absorption efficiency:** The perovskite layer is renowned for its remarkable ability to absorb light efficiently, enabling the conversion of a significant portion of sunlight into electrical energy.
- ✓ **Manufacturing simplicity:** Compared to other materials used in solar cells, the perovskite layer is simpler to manufacture and integrate, resulting in reduced production costs.

✓ **High conversion efficiency:** Research indicates that the perovskite layer demonstrates excellent efficiency in converting sunlight into electrical power.

In most cases, the perovskite layer is combined with additional layers in multilayer solar cell structures to improve both stability and energy conversion performance. Perovskite technology is considered one of the most groundbreaking advancements in solar energy, representing a major step forward in enhancing the efficiency of solar cells [2].

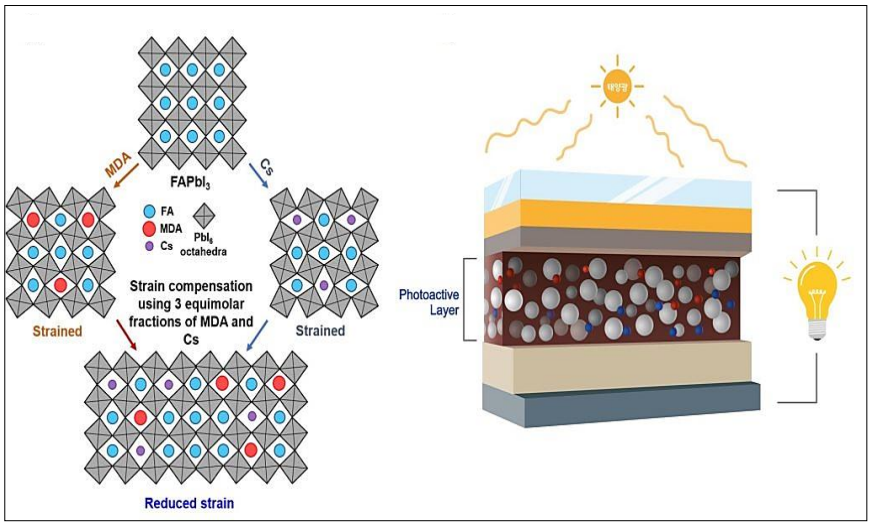

***Figure 2.1**: Shows the general cubic crystal structure of perovskites.*

2.2.1. Composition and Components of Perovskite structure

As previously mentioned, the perovskite materials in solar cells consists of a blend of organic and inorganic materials. The perovskite structure follows the general formula ABX_3 [11], where:

- **A** is an organic or inorganic monovalent cation, typically methylammonium ($CH_3NH_3^+$), formamidinium ($CH(NH_2)_2^+$), cesium (Cs^+), or potassium (K^+) etc.
- **B** is an inorganic cation, usually a metal like lead (Pb^{2+}) or tin (Sn^{2+}), etc.
- **X** is a halide anion, such as chloride (Cl^-), bromide (Br^-), or iodide (I^-), etc.

a) Organic Materials:

✓ **Methylammonium ($CH_3NH_3^+$):** A common organic cation used in many perovskite formulations.

✓ **Formamidinium ($CH(NH_2)_2^+$):** Another organic cation that can be used to improve stability and efficiency.

- ✓ **Polymeric Hole Transport Materials (HTMs):** Organic materials such as Spiro-OMeTAD, PEDOT, etc., are often used to transport holes in the perovskite structure.

b) Inorganic Materials:

- ✓ **Lead (Pb^{2+}):** The most common metal cation used in perovskite solar cells, forming compounds like methylammonium lead iodide ($CH_3NH_3PbI_3$).
- ✓ **Tin (Sn^{2+}):** Used as an alternative to lead, though it is less stable.
- ✓ **Cesium (Cs^{+}):** An inorganic cation used to enhance the stability of the perovskite structure.
- ✓ **Halide Anions (Cl^{-}, Br^{-}, I^{-}):** These halides form the X component of the ABX_3 structure and are crucial in determining the optical and electrical properties of the perovskite [1,11].

These components combine to create a highly effective and adaptable light-absorbing layer in perovskite solar cells.

2.2.1.1. Rubidium Tin Iodide ($RbSnI_3$)

The perovskite research community has shown increasing interest in $RbSnI_3$ as a potential alternative to other toxic and expensive materials, such as $MAPbI_3$, $CsPbI_3$, and $KsnI_3$, commonly used in photovoltaic devices [11]. $RbSnI_3$ is particularly characterized by its low toxicity and promising optoelectronic properties, including a direct band gaps of 0.828 eV and high light absorption efficiency. These features make $RbSnI_3$ a strong candidate for use in solar cells.

This compound is synthesized by combining rubidium (Rb^{+}), tin (Sn^{+}), and iodide (I^{-}) ions, forming a stable perovskite structure. Its rhombohedral crystal geometry plays a key role in its excellent optical and electronic properties [15], making it a valuable material in the development of solar energy technologies as shown in Figure 2.2.

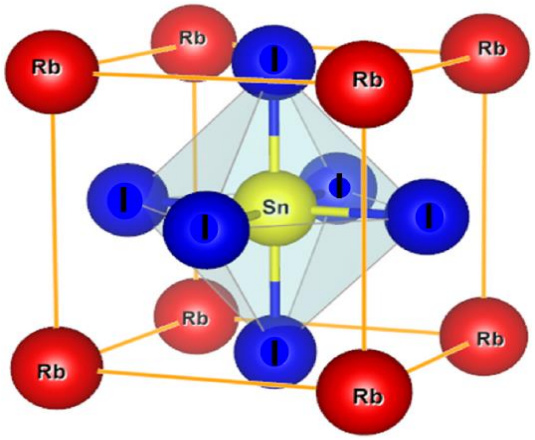

Figure 2.2: *The crystal structure of $RbSnI_3$.*

As a newly emerging material, $RbSnI_3$ has not been comprehensively studied, and no experimental studies on perovskite solar cells (PSCs) using $RbSnI_3$ have been documented in the current literature. However, theoretical research offers some promising insights. For example, Harun-Or-Rashid et al. performed DFT analysis of $RbSnI_3$ and, using the SCAPS simulator, proposed a novel single-junction $RbSnI_3$ solar cell, achieving a power conversion efficiency (PCE) of 32% [3]. Additionally, Sarkar et al. demonstrated that a Cu-doped $RbSnI_3$ device achieves a PCE of 20.2%. The Cu doping in $RbSnI_3$ increases the bond length, which reduces exciton binding energy and enhances charge carrier generation [16]. Despite these developments, studies focusing on $RbSnI_3$-based perovskite solar cells are still rare, with only a limited number of theoretical investigations reported so far.

2.2.1.2. Rubidium Tin Bromide ($RbSnBr_3$)

Rubidium tin bromide ($RbSnBr_3$) is an inorganic halide perovskite composed of rubidium (Rb), tin (Sn), and bromine (Br), as shown in Figure 2.3. $RbSnBr_3$ adopts the general ABX_3 perovskite structure, where Rb occupies the A site, tin (Sn) the B site, and bromine (Br) the X site. This lead-free perovskite has emerged as a promising candidate in the photovoltaic field, particularly for perovskite solar cells (PSCs) [4], due to its non-toxic nature and favorable optoelectronic properties. Unlike lead-based perovskites, $RbSnBr_3$ avoids the environmental and health concerns associated with lead, making it a sustainable alternative for next-generation solar energy applications.

Recent research has highlighted the tunable electronic and optical properties of $RbSnBr_3$, which are influenced by its crystal structure and composition. The material typically has a cubic structure (space group Pm-3m) in its highly symmetric phase, although it can also adopt an orthorhombic or triclinic phase, depending on temperature and synthesis conditions. The band gap of $RbSnBr_3$ varies across its phases, with reported values ranging from approximately 0.8 to 1.5 eV [5], depending on the crystal structure and computational methods used. For example, the orthorhombic phase has been observed to have a larger band gap, which enhances its light absorption in the UV-vis range, which is beneficial for photovoltaic and optoelectronic applications.

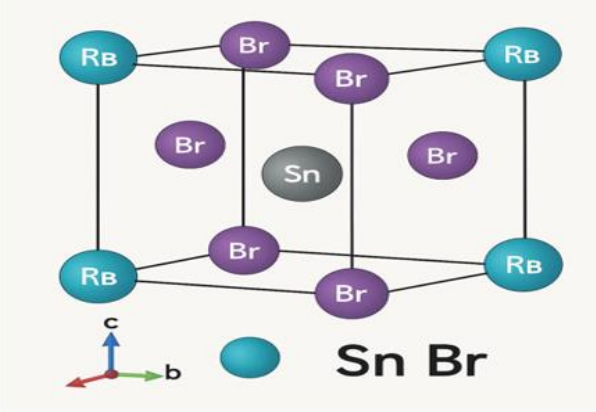

Figure 2.3: *The crystal structure of unit cell of $RbSnBr_3$.*

There are not enough studies on this topic; however, recent research has been conducted on perovskite solar cells (PSCs) based on $RbSnBr_3$. Theoretically, using $RbSnBr_3$ in a single-junction configuration, Harun-Or-Rashid et al. achieved remarkable efficiency with structures such as FTO/SnS_2/$RbSnBr_3$/Au. Their work demonstrated potential efficiencies exceeding 29.79% [3], highlighting the material's versatility and effectiveness for photovoltaic applications.

2.2.1.3. Tin disulfide (SnS_2)

In nature, tin disulfide (SnS_2) occurs as part of minerals such as Bernardtite. SnS2 has a hexagonal crystal unit cell, with a crystal structure similar to that of layered chalcogenides. The lattice constants, a = 5.899 Å and b = 3.648 Å, reflect the layered nature of the structure, where atoms within the layers are held together by strong covalent bonds, while the attractive forces between the layers are weak (van der Waals forces).

Figure 2.4 (schematic) shows the crystal structure of SnS_2, where each tin (Sn) atom is located at the geometric center of six sulfur (S) atoms, forming a distorted triangular prism. The layers are stacked on top of each other along the c-axis. Gaps between the layers allow for easy mechanical separation of the layers. SnS_2, used in this experiment with a bandgap of 2.24 eV, is a highly promising material for highly efficient photovoltaics due to its wide bandgap and excellent electron mobility in the visible light spectrum [6]. This enhances the efficiency of carrier transport from the active layer to the electrode, improving the overall performance of the device [9, 10]. The electrical and optical properties of SnS_2 can be improved by doping with elements such as iron (Fe), cobalt (Co), nickel (Ni), and silver (Ag), which tunes the electronic conductivity or controls the bandgap properties.

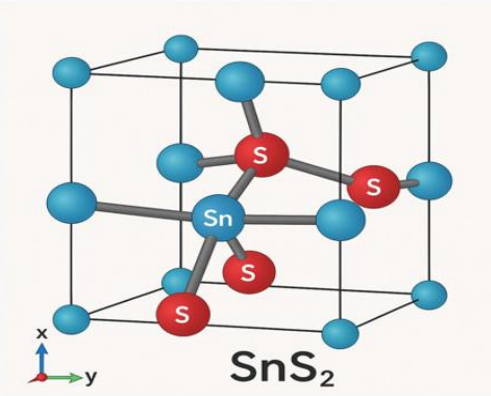

Figure 2.4: *The crystal structure of unit cell of SnS_2.*

2.2.1.4. Cadmium Sulfide (CdS)

In nature, cadmium disulfide (CdS) occurs in minerals such as greenockite. CdS has a hexagonal crystalline cell, with a crystal structure similar to layered chalcogenides. This layered structure is characterized by strong covalent bonds between atoms within the layers, while interlayer forces (van der Waals) are weak. Figure 2.5 (illustration) shows the CdS crystal structure, where each cadmium (Cd) atom is located at a geometric center surrounded by six sulfur (S) atoms, forming a distorted triangular prism. The layers are stacked on top of each other along the c-axis. Spacers between the layers allow them to be easily mechanically separated. CdS has a wide band gap of 2.42 eV at room temperature, usually, the undoped CdS has naturally n-type conductivity because of native defects of sulfur (S) vacancies [17]. CdS, used in this study, is a very promising material for high-efficiency solar cells due to its wide energy gap and high electron mobility in the visible light range. This improves the efficiency of carrier transport from the active layer to the electrode, thus enhancing overall device performance. The electrical and optical properties of CdS can be tailored by doping with elements such as zinc (Zn), indium (In), or aluminum (Al), enabling modification of the electronic conductivity or control of the energy gap properties.

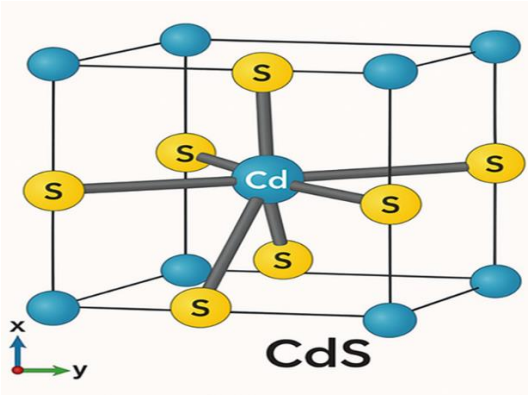

Figure 2.5: *The crystal structure of unit cell of CdS.*

2.3.The simulation

Solar cell simulation software consists of advanced computational tools designed to model and evaluate the performance of solar cells under various operating conditions. These programs simulate the behavior of solar cells by accounting for factors such as light intensity, temperature, and the material properties used in their construction. Through the use of detailed physical and mathematical models—such as charge balance equations, transport equations, and continuity equations—the software can accurately predict the efficiency and electrical performance of a solar cell under diverse scenarios. These simulation tools are invaluable for enhancing the understanding of solar cell mechanisms and optimizing their design. They enable researchers and engineers to test new design concepts or modify cell parameters virtually, without the need for physical prototypes, significantly reducing time and development costs. Some of the most widely used solar cell simulation software includes SCAPS, Silvaco, PC1D, Centaurus TCAD, among others. These platforms provide user-friendly yet highly versatile interfaces, facilitating precise analysis and detailed studies of solar cell performance for researchers and engineers alike.

2.3.1. SCAPS-1D

SCAPS-1D (Solar Cell Capacitance Simulator) is a one-dimensional solar cell device simulation tool developed by the Electronics and Information Systems (ELIS) department at the University of Ghent under the guidance of M. Burgelman [12]. The software is freely available to the photovoltaic research community. SCAPS models a solar cell as a stack of up to seven layers, each defined by specific properties such as thickness, doping levels, optical absorption, defect densities, and defect distribution. The software allows for the simulation of key parameters, including I-V, QE, C-V, and C-f characteristics. SCAPS-1D is widely regarded for its ability to produce simulation results that align closely with experimental data. In this study, SCAPS-1D version 3.3.07 was employed, chosen for its user-friendly interface, ease of control, the capability to simulate both illuminated and dark conditions, and its ability to design heterostructure systems with up to seven layers [13].

2.3.1.1. Simulation equations

To obtain accurate results, the SCAPS software uses a one-dimensional diffusion system to solve Poisson's and continuity equations, taking into account the boundary conditions. This method allows for an accurate representation of the internal electric field and carrier behavior within the cell [7]. The most important of these equations that the program follows are:

- **Poisson's Equation:** Equation (2.1) defines Poisson's equation, which describes the relationship between electrostatic potential and charge density [7,8,13].

$$\frac{\partial^2}{\partial^2 x}\varphi(x) = \frac{q}{\varepsilon_r}[p(x) - n(x) + N_D^+(x) - N_A^-(x) \pm N_t(x)\,] \qquad (2.1)$$

In this context, the electrostatic potential is represented by φ, the charge by q , and the static relative permittivity of the medium by ε_r. The electron and hole concentrations are denoted by n and p, respectively, while the donor and acceptor densities are symbolized as $N_D^+$and N_A^-. Furthermore, the defect densities of acceptors and donors are indicated by N_t.

- **Continuity equations:** The continuity equations express a fundamental principle: the variation in carrier density over time is governed by the balance between incoming and outgoing carrier flux, combined with the processes of generation and recombination. The continuity equations for electrons and holes are mathematically expressed as follows [7,8,13]:

Continuity equation for the electron: $$\frac{\partial n}{\partial t} = \frac{1}{q}\frac{\partial J_n}{\partial x} + G_n - R_n \qquad (2.2)$$

Continuity equation for the hole: $$\frac{\partial p}{\partial t} = \frac{1}{q}\frac{\partial J_p}{\partial x} + G_p - R_p \qquad (2.3)$$

Where J_n and J_p represent the current densities of electrons and holes, G_n and G_p denote the carrier generation rates for electrons and holes, and R_n and R_p represent the recombination rates of electrons and holes, respectively.

- **Transport equation:** Similarly, the carrier current density can be determined using the following transport equations for drift-diffusion (total current density) [7,8,14]:

$$J_n = nq\mu_n E + qD_n\frac{\partial n}{\partial x} \qquad (2.4)$$

$$J_p = pq\mu_p E + qD_p\frac{\partial p}{\partial x} \qquad (2.5)$$

Here, μ_n and μ_p refer to the mobilities of electrons and holes, respectively, while D_n and D_p denote the diffusion coefficients for electrons and holes, respectively. $\frac{\partial n}{\partial x}$ and $\frac{\partial p}{\partial x}$ represent the concentration gradients of electrons and holes, respectively.

2.3.1.2. Essential Steps for Conducting a Successful SCAPS Simulation

To achieve a successful simulation in SCAPS, follow these essential steps:

a) After we install the program on the computer, we click on the program icon to open it, and the main interface appears, as shown in Figure 2.6.

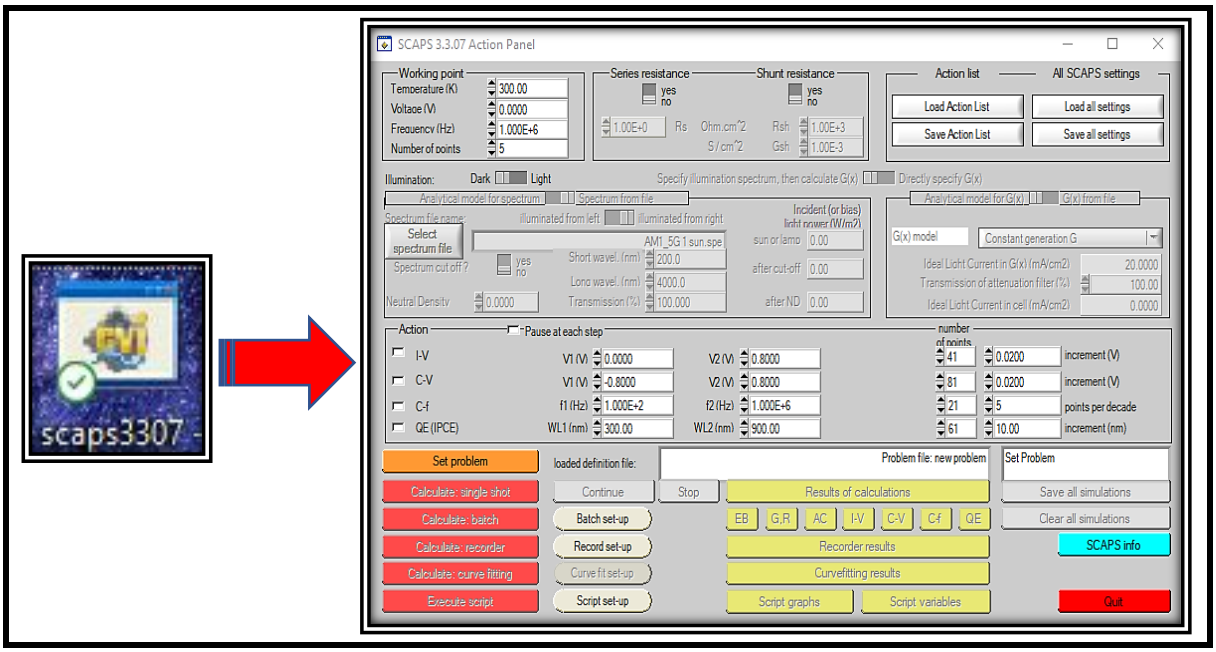

Figure 2.6: *The application's icon and main window.*

b) The scene is first adjusted from dark to light (1). Then, the criteria to be analyzed and their respective ranges are defined (2,3). Subsequently, the "Set Problems" option is selected to input the materials and their properties (4), as illustrated in Figure 2.7.

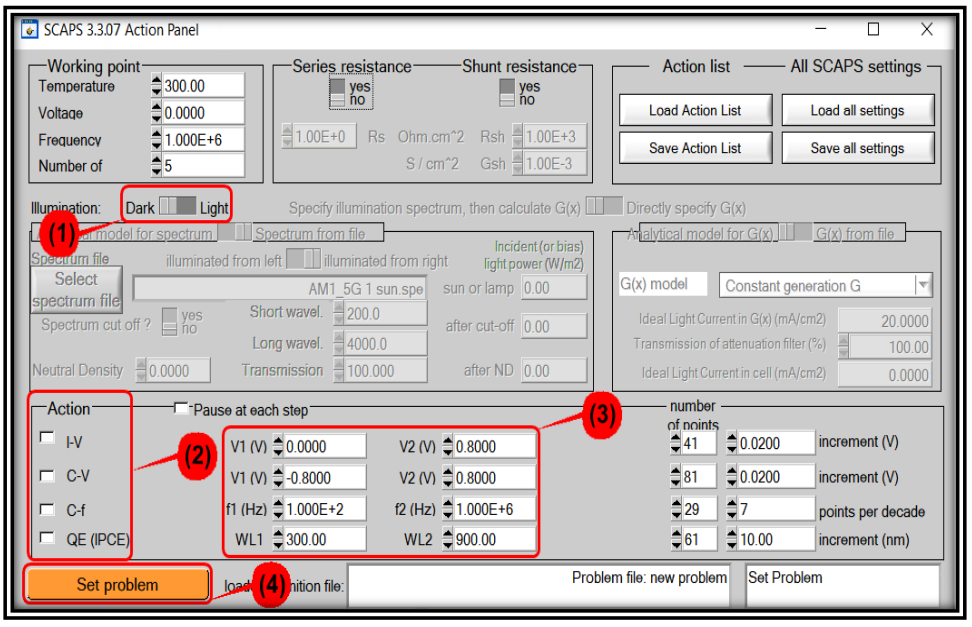

Figure 2.7: *Initial Steps for Running the Simulation.*

c) Selecting the 'Set Problems' option opens a new interface in the software. Within this interface, additional cell elements can be incorporated by expanding the layers section, as depicted in Figure 2.8. The arrows on the white box containing the cell indicate the direction of sunlight.

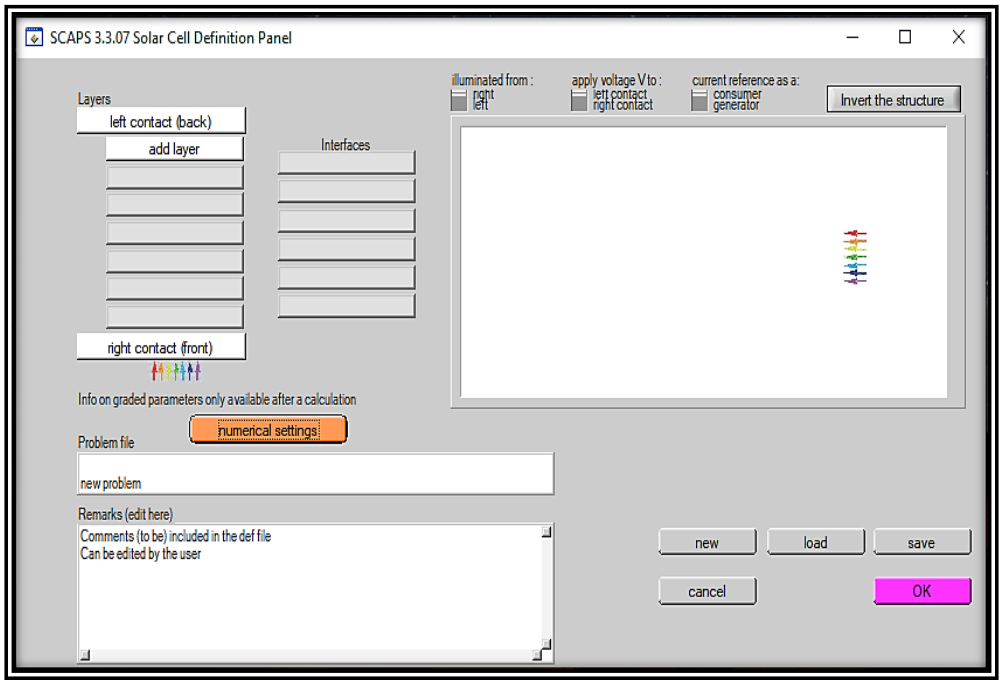

Figure 2.8: *A window for entering cell elements.*

d) As illustrated in Figure 2.8, there is a designated layered section. To add a layer, click the "Add Layer" button, which opens a new interface (see Figure 2.9). Here, you can input the material properties, such as thickness, bandgap, electron affinity, and more. After entering the details, click the "Add" button to successfully include the material. Repeat this process for the remaining materials. If the material and its properties are already stored in the program's database, you can load them by selecting the "Load Materials" button. For optical properties, use the "Set Absorption Model" button or import them directly from a file. To introduce defects, click the "Add Defect 1" button.

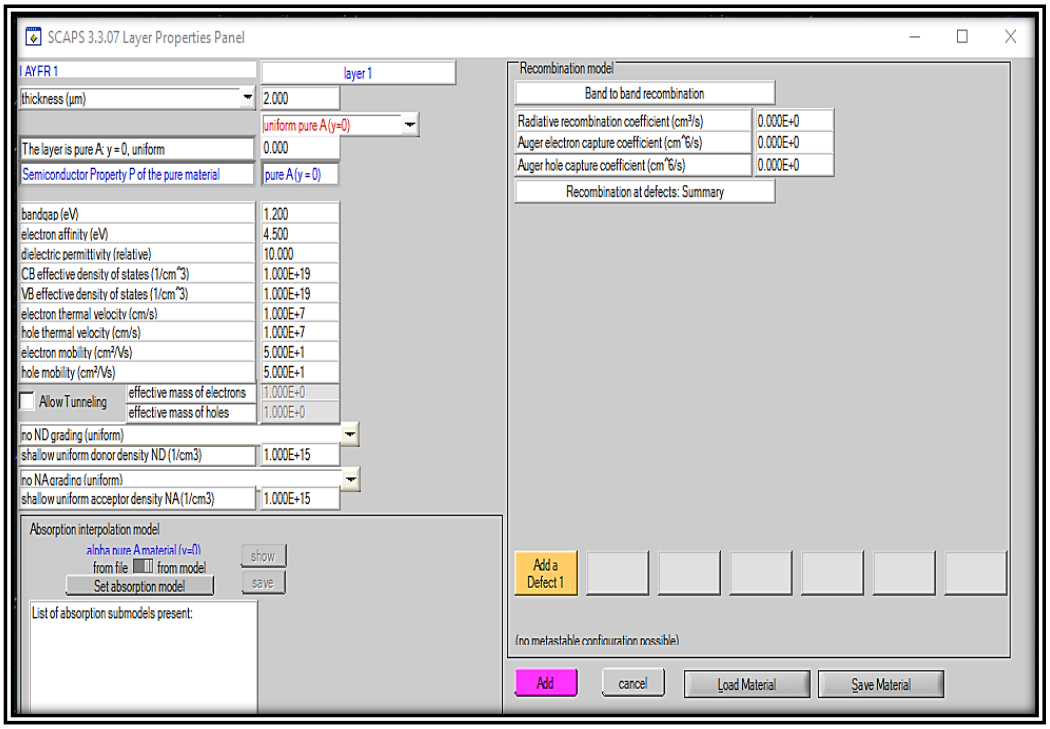

Figure 2.9: *Creating cell layers and their properties.*

e) The characteristics of the front and rear contacts—such as thermionic emission, surface recombination velocity, and metal work function—can be modified by selecting the respective contact button in the cell definition section (refer to Figure 2.10). This will open the 'Contact Properties Panel', as illustrated in Figure 2.11.

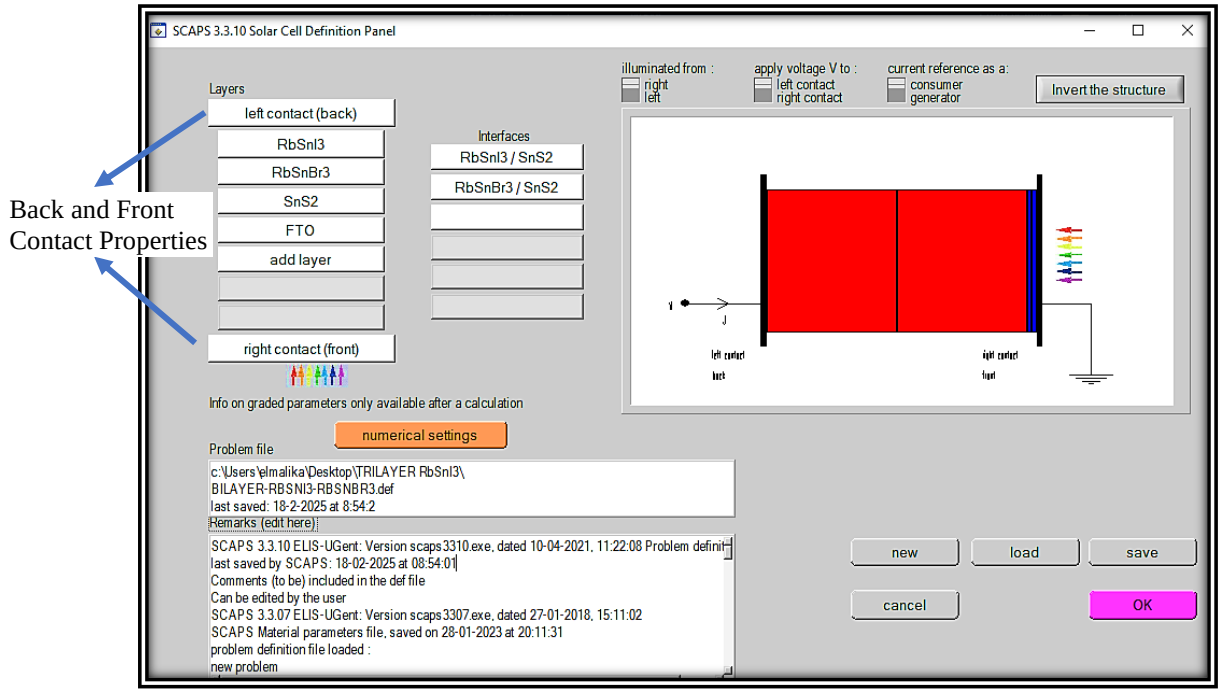

Figure 2.10: *Varying the Left and Back Contact Properties.*

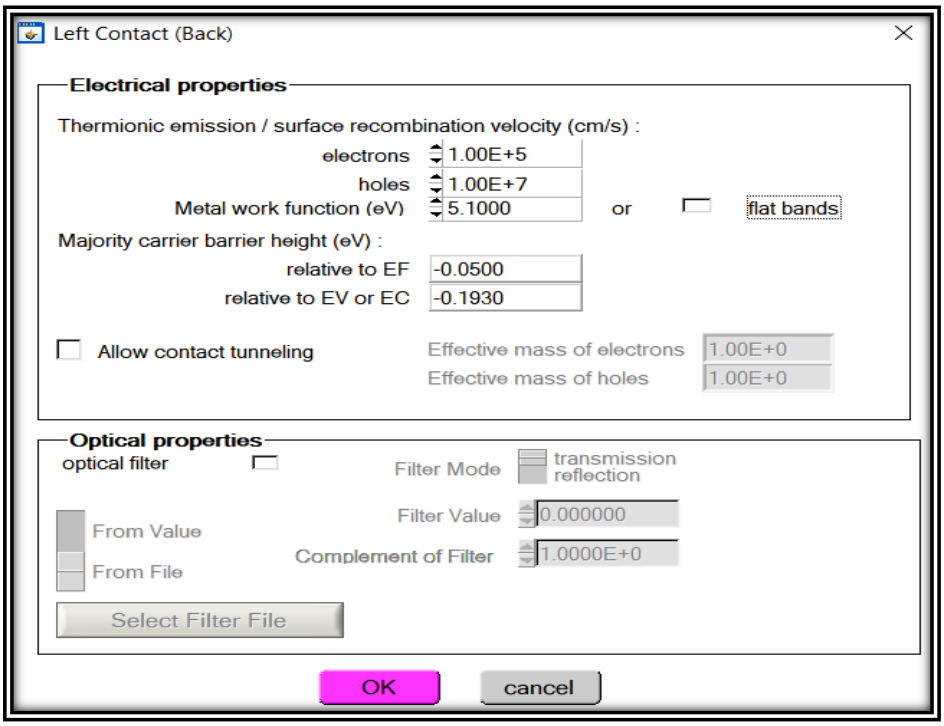

Figure 2.11: *Interface for Configuring Contact Parameters.*

f) After assembling all the required components to form the complete solar cell structure, the configuration can be saved by clicking the "Save" option. To begin the simulation, return to the main interface (see Figure 2.6) and select the "Calculate" button to initiate the process.

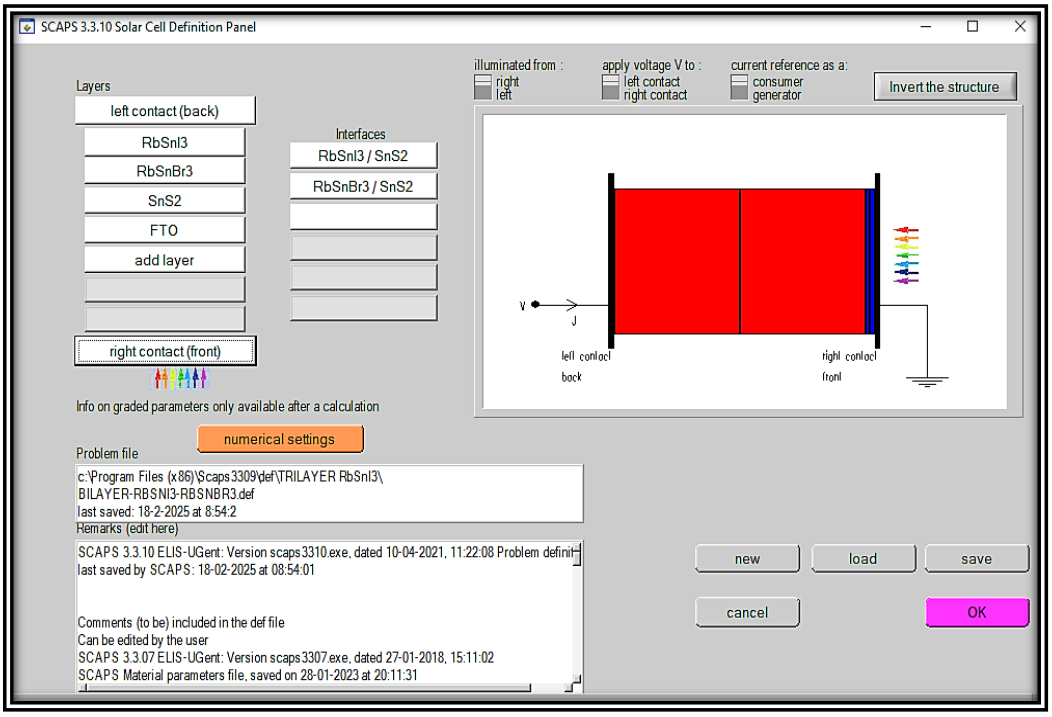

Figure 2.12: *Simulation Example of the Designed FTO/SnS_2/$RbSnBr_3$/$RbSnI_3$ Bilayer PSC Structure.*

2.4.Conclusion

In this chapter, we explored the fundamental aspects of perovskite solar cells, focusing on the structure, composition, and unique properties of the materials used in our simulations. Particular attention was given to lead-free halide perovskites such as $RbSnI_3$ and $RbSnBr_3$, as well as additional layers including SnS_2 and CdS, each contributing to the efficient operation of the solar cell. These materials exhibit excellent optoelectronic properties, such as strong light absorption and high charge carrier mobility, making them ideal candidates for next-generation photovoltaic applications.

We then introduced the SCAPS-1D simulation software as a powerful tool for modeling and analyzing solar cell performance. Key simulation equations and parameters were discussed, along with a step-by-step methodology for setting up and conducting simulations. This provides the foundational knowledge required to accurately interpret results and optimize device structures for maximum efficiency.

Together, the detailed material characterization and the simulation framework presented in this chapter establish a solid basis for the design and evaluation of high-performance perovskite-based solar cells. This knowledge is essential for the subsequent analysis and optimization of device architectures in the following chapters.

References Chapter 2 :

[1] Miyasaka, Tsutomu, et al. "Perovskite solar cells: can we go organic-free, lead-free, and dopant-free?." Advanced Energy Materials 10.13 (2020): 1902500.

[2] Kojima, Akihiro, et al. "Organometal halide perovskites as visible-light sensitizers for photovoltaic cells." Journal of the american chemical society 131.17 (2009): 6050-6051.

[3] Harun-Or-Rashid, M., Rahman, M. F., Amami, M., Farhat, L. B., Islam, M. M., & Benami, A. (2025). Exploring new lead-free halide perovskites RbSnM3 (M= I, Br, Cl) and achieving power conversion efficiency> 32%. Journal of Physics and Chemistry of Solids, 197, 112437.

[4] Bhari, B. Z., Rahman, K. S., Chelvanathan, P., & Ibrahim, M. A. (2023). Plausibility of ultrathin CdTe solar cells: probing the beneficial role of MgZnO (MZO) high resistivity transparent (HRT) layer. *Journal of Materials Science*, *58*(40), 15748-15761.

[5] Rahman, M. H., Jubair, M., Rahaman, M. Z., Ahasan, M. S., Ostrikov, K. K., & Roknuzzaman, M. (2022). RbSnX 3 (X= Cl, Br, I): promising lead-free metal halide perovskites for photovoltaics and optoelectronics. *RSC advances*, *12*(12), 7497-7505.

[6] Rahman, M. F., Harun-Or-Rashid, M., Islam, M. R., Irfan, A., Chaudhry, A. R., Rahman, M. A., & Al-Qaisi, S. (2024). A Deep Analysis and Enhancing Photovoltaic Performance Above 31% with New Inorganic RbPbI3-Based Perovskite Solar Cells via DFT and SCAPS-1D. *Advanced Theory and Simulations*, *7*(10), 2400476.

[7] Mohammed, M. K., Al-Gazally, M. E., Khaleel, O. A., Al-Mousoi, A. K., Jeddoa, Z. M. A., Majdi, H. S., ... & Dastan, D. (2024). Improved eco-friendly CsSn 0.5 Ge 0.5 I 3 perovskite photovoltaic efficiency beyond 20% with SMe-TATPyr hole-transporting layer. *Physical Chemistry Chemical Physics*, *26*(4), 3229-3239.

[8] S.M. Sze, M.-K. Lee, Semiconductor Devices: Physics and Technology: Physics and Technology, Wiley Global Education, 2012.

[9] Ghebouli, M. A., Ghebouli, B., Larbi, R., Chihi, T., & Fatmi, M. (2021). Effect of buffer nature, absorber layer thickness and temperature on the performance of CISSe based solar cells, using SCAPS-1D simulation program. *Optik*, *241*, 166203.

[10] Reza, M. S., Rahman, M. F., Kuddus, A., Mohammed, M. K., Pal, D., Ghosh, A., ... & Amami, M. (2024). Design and optimization of high-performance novel RbPbBr3-based solar cells with wide-band-gap S-Chalcogenide electron transport layers (ETLs). *ACS omega*, *9*(18), 19824-19836.

[11] Ri, C. H., Kim, Y. S., Jong, U. G., Kye, Y. H., Ryang, S. H., & Yu, C. J. (2021). First-principles study on structural, electronic and optical properties of perovskite solid solutions KB 1− x Mg x I 3 (B= Ge, Sn) toward water splitting photocatalysis. *RSC advances*, *11*(42), 26432-26443.

[12] Burgelman, M., Nollet, P., & Degrave, S. (2000). Modelling polycrystalline semiconductor solar cells. Thin solid films, 361, 527-532.

[13] Pindolia, G., Shinde, S. M., & Jha, P. K. (2022). Optimization of an inorganic lead free RbGeI3 based perovskite solar cell by SCAPS-1D simulation. *Solar Energy*, *236*, 802-821.

[14] Rahman, M. F., Moon, M. M. A., Hossain, M. K., Ali, M. H., Haque, M. D., Kuddus, A., ... & Ismail, A. B. M. (2022). Concurrent investigation of antimony chalcogenide (Sb2Se3 and Sb2S3)-based solar cells with a potential WS2 electron transport layer. *Heliyon*, *8*(12).

[15] Khan, K., Sahariya, J., & Soni, A. (2021). Structural, electronic and optical modeling of perovskite solar materials ASnX3 (A= Rb, K; X= Cl, Br): first principle investigations. *Materials Chemistry and Physics*, *262*, 124284.

[16] Sarkar, J., Chaki, T., Mandal, P. K., & Chatterjee, S. (2024). Effect of metal (Cr, Sr, Ag, Cu) doping on the performance of lead-free RbSnI3 based perovskite solar cells: A theoretical approach. *Physica Scripta*, *99*(5), 055932.

[17] TINEDERT, I. E. (2022). *Numerical simulation of the performance of solar cells formed by nanostructures based on II-VI semiconductors (Simulation numérique des performances des cellules solaires formées par des nanostructures à base des semi-conducteurs II-VI)* (Doctoral dissertation, Faculté des Sciences et de la technologie).

Chapter 03: Analysis and Interpretation of Numerical Simulation Results

3.1.Introduction

In this chapter, we present a comprehensive analysis of single-layer and bilayer perovskite solar cells through one-dimensional numerical simulations using the SCAPS-1D software. As a starting point, we simulate a reference single-layer structure—FTO/SnS_2/$RbSnI_3$/Spiro/Au—previously proposed by *Md. Harun-Or-Rashid et al*. (2025) based on numerical modeling. This structure employs a lead-free halide perovskite absorber of the $RbSnM_3$ family (M = I, Br, Cl). Our simulation results show a strong agreement with those reported in the original study, confirming the reliability of our simulation approach.

Despite the promising performance of this single-absorber configuration, the overall power conversion efficiency remains constrained. To address this limitation, we propose a bilayer architecture by introducing $RbSnBr_3$ as an additional top absorber layer, forming the structure FTO/SnS_2/$RbSnBr_3$/$RbSnI_3$/Spiro/Au. By comparing the performance metrics of the single and bilayer devices, we highlight the impact of the bilayer design on solar cell efficiency. Subsequently, we proceed to optimize the bilayer perovskite solar cell by evaluating various electron transport layers (ETLs) suitable for the bilayer structure. Additionally, we systematically vary critical parameters such as layer thicknesses, doping concentrations, and the influence of different back contact metals. Through this comprehensive parametric study, we determine the most efficient configuration for the $RbSnBr_3$/$RbSnI_3$ bilayer system. The findings of this chapter lead to the identification of an optimized device architecture for bilayer lead-free perovskite solar cells.

3.2.Structures of PSCs and Simulation parameters used

Perovskite solar cells (PSCs) are typically composed of multiple functional layers, each with a specific role in ensuring efficient photovoltaic operation. A schematic representation of a typical device architecture is shown in Figure 3.1. The performance and power conversion efficiency (PCE) of a PSC largely depend on the properties and interaction of these layers. The key components of the device structure include the absorber layer, electron transport layer (ETL), hole transport layer (HTL), and the front and back electrodes.

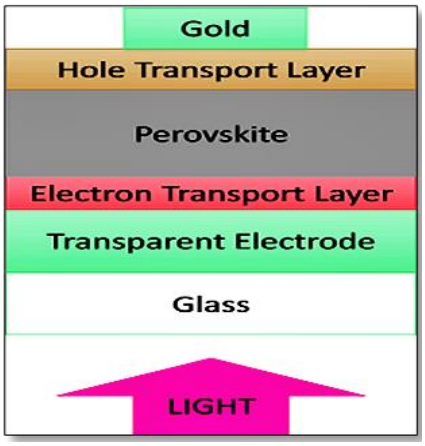

Figure 3.1: *Common Design Configurations in Perovskite Solar Cells.*

- **Absorber Layer**

The absorber layer serves as the core component of the perovskite solar cell, where incident photons are captured, leading to the creation of electron-hole pairs. This layer is fundamental because it governs the effectiveness of photon harvesting and the subsequent production of charge carriers, which are then directed toward the electron transport layer (ETL) and hole transport layer (HTL).

- **Electron Transport Layer (ETL)**

The electron transport layer in a solar cell plays a crucial role by facilitating the efficient transfer of electrons from the active layer to the electrode, while simultaneously blocking the movement of holes toward the electrode. This layer significantly contributes to improving the overall efficiency of the cell by minimizing energy losses and enhancing the rate of charge transport [2].

- **Hole Transport Layer (HTL)**

The Hole Transport Layer (HTL) in a photovoltaic device serves the essential function of selectively conducting holes from the photoactive layer to the anode, while simultaneously impeding the passage of electrons toward the electrode. By optimizing charge separation and minimizing recombination losses, the HTL plays a pivotal role in enhancing the power conversion efficiency and overall performance of the solar cell [2].

- **Transparent and metallic electrode**

The front electrode, usually composed of transparent conductive oxides (TCOs) like fluorine-doped tin oxide (FTO) or indium tin oxide (ITO), allows light to pass through to the absorber layer while also conducting charge carriers laterally across the device. The back contact is typically made of metals such as gold (Au) or aluminum (Al), which provide excellent

electrical conductivity for the efficient collection of holes from the HTL. Together, these electrodes ensure effective charge extraction and contribute to the stability and efficiency of the solar cell [1,9].

In this investigation, our objective was to explore the operational mechanisms of $RbSnBr_3/RbSnI_3$ bilayer perovskite solar cells (PSCs). To achieve this, we initially conducted simulations on the performance of a single-junction $RbSnI_3$-based PSC. Subsequently, we examined the behavior and efficiency of a $RbSnBr_3/RbSnI_3$ bilayer PSC. By systematically comparing the outcomes of these two device architectures, we aimed to assess and elucidate the role and significance of incorporating dual absorber layers within the cell structure. Figures 3.2 (a) and (b) illustrate the schematic representations of the reference single-junction $RbSnI_3$ PSC and the $RbSnBr_3/RbSnI_3$ bilayer PSC, respectively. Both device architectures employ fluorine-doped tin oxide (FTO) as the transparent front contact and gold (Au) as the rear metallic electrode. The electron transport layer (ETL) is composed of tin disulfide (SnS_2). The primary distinction between the two configurations lies in the absorber layer design. In the single-junction structure (Figure 3.2 (a)), $RbSnI_3$ is solely utilized as the active absorber layer. Conversely, the bilayer structure (Figure 3.2 (b)) incorporates a heterojunction composed of two perovskite materials: $RbSnBr_3$ as the Top absorber layer and $RbSnI_3$ as the Bottom layer. Figure 3.3 presents the band diagrams of the bilayer structure, highlighting the two absorber layers, $RbSnBr_3$ and $RbSnI_3$. This bilayer design aims to broaden the absorption spectrum and enhance carrier separation by leveraging the complementary optoelectronic properties of both materials. The physical and electrical parameters used in the numerical simulations for each layer in the single-layer and bilayer PSCs are summarized in Table 3.1.

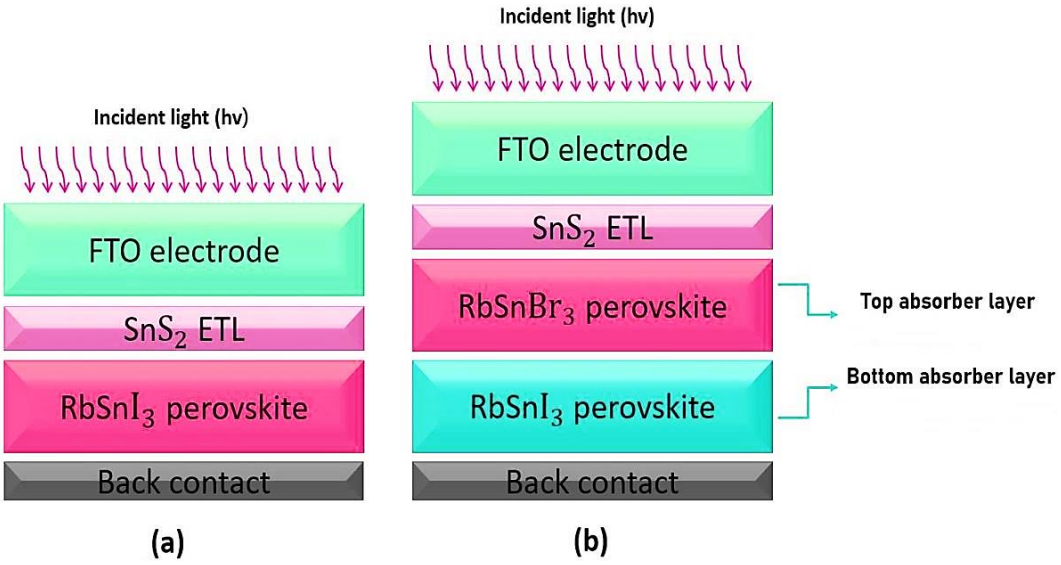

Figure 3.2: *Structure of (a) a single-layer PSC [3] and (b) a proposed bilayer PSC.*

Table 3.1: Material Parameters Used in SCAPS Simulations for Single and Bilayer Perovskite Solar Cells.

Parameters	**Layers**			
	FTO	**SnS_2**	**$RbSnBr_3$**	**$RbSnI_3$**
Thickness, t_m (nm)	20	30	750	750
Bandgap, E_g (eV)	3.6	2.4	0.988	0.828
Electron affinity, χ_e (eV)	4.5	4.24	3.95	3.8
Dielectric ratio, E_{ps}	10	10	8.6	10.9
Electron mobility, μ_n (cm^2/Vs)	100	20	50	45
Hole mobility, μ_p (cm^2/Vs)	20	10	50	55
Valence band density of states, N_v (cm^{-3})	1.8×10^{19}	1.8×10^{19}	1.205×10^{19}	2.8×10^{19}
Conduction band density of states, N_c (cm^{-3})	2×10^{18}	2.2×10^{18}	1.89×10^{18}	1.4×10^{19}
Donor concentration, N_d (cm^{-3})	1×10^{17}	1×10^{16}	-	-
Acceptor concentration, N_a (cm^{-3})	-	-	1×10^{16}	1×10^{16}
Defect Density, N_t (cm^{-3})	1×10^{14}	1×10^{14}	1×10^{12}	1×10^{12}

To accurately model the interfaces in perovskite solar cell structures, interface defect states were introduced at the ETL/$RbSnI_3$, ETL/$RbSnBr_3$, and $RbSnBr_3$/$RbSnI_3$ junctions. These interface defects were considered to be neutral in nature, with both electron and hole capture cross sections set to 1.00×10^{-19} cm^2. A single energetic distribution was used, with the defect energy level referenced 0.600 eV above the highest valence band edge (EV). The characteristic energy was chosen as 0.100 eV, and the total defect density was set to $1.00 \times 10^{10} cm^{-2}$ [3].

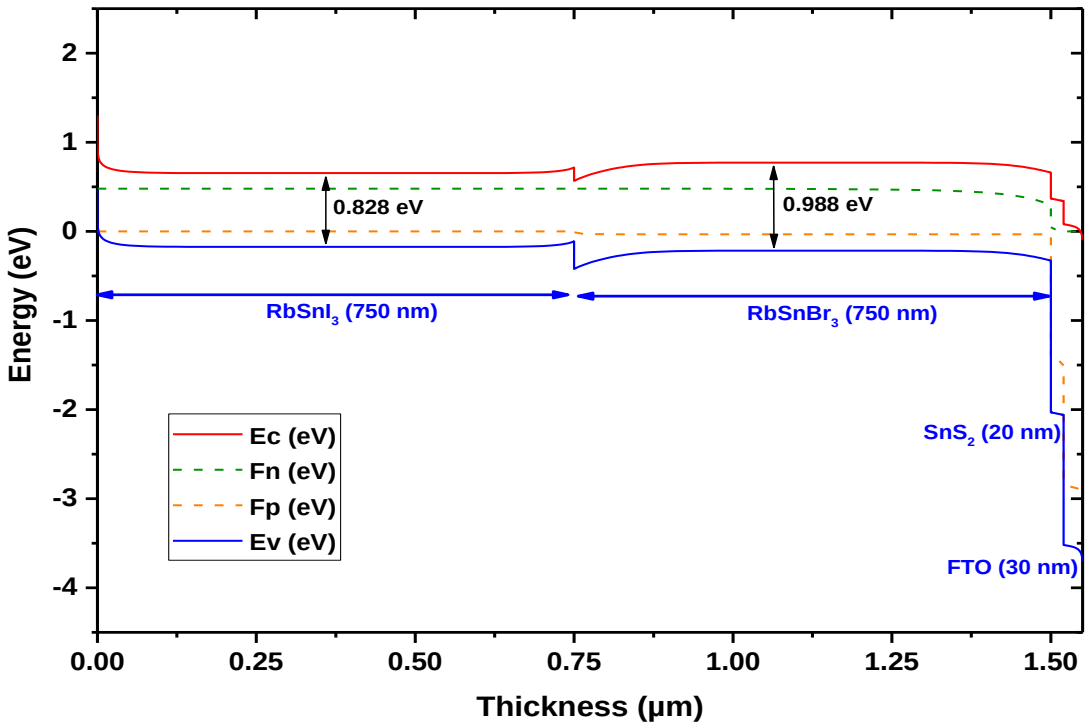

Figure 3.3: Band alignment of a $RbSnBr_3$/$RbSnI_3$ bilayer solar cell.

3.3.Simulation results

The simulation study began with a single-junction perovskite solar cell (PSC) based on $RbSnI_3$, followed by the design and analysis of a bilayer structure incorporating both $RbSnBr_3$ and $RbSnI_3$ as absorber layers, as illustrated in Figure 3.2. Figures 3.4 and 3.5 present the comparative simulation results for the single-junction and bilayer PSC configurations. The single-junction $RbSnI_3$-based PSC achieved a power conversion efficiency (PCE) of 26.50%, as extracted from the current–voltage (J–V) characteristics shown in Figure 3.4. Notably, these results align closely with prior numerical data reported in the literature [3], confirming the accuracy and reliability of the simulation methodology adopted in this work.

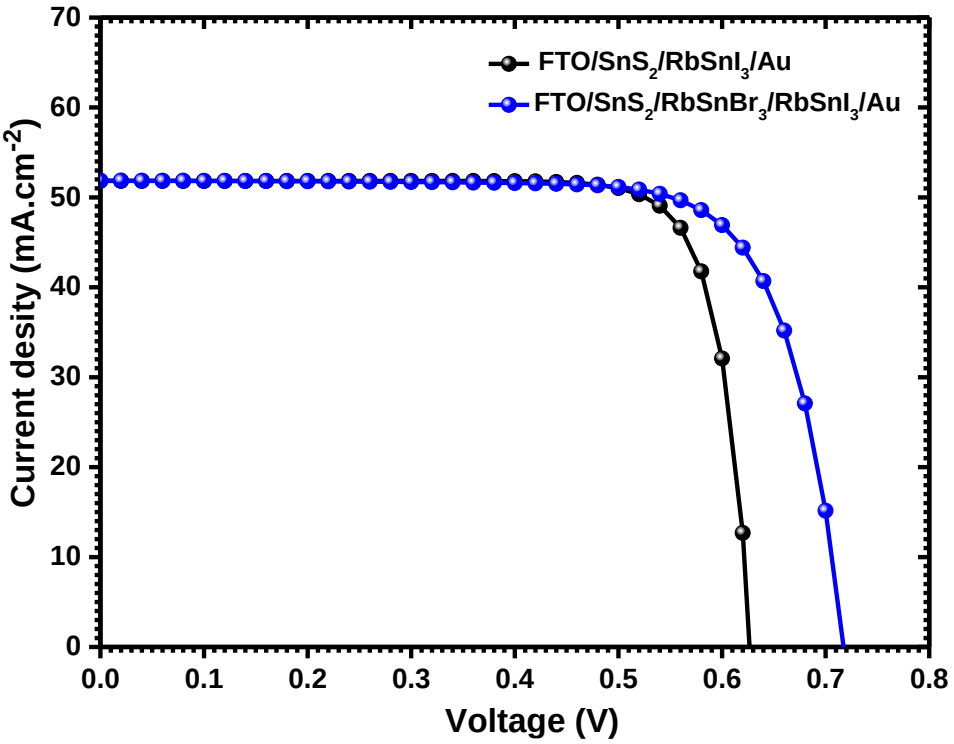

Figure 3.4: Comparison of J–V Characteristics for $RbSnI_3$ Single-Junction PSC and $RbSnBr_3$/$RbSnI_3$ Bilayer PSC.

The bilayer PSC configuration, which utilizes $RbSnBr_3$ as the top absorber layer and $RbSnI_3$ as the bottom layer, demonstrated improved performance compared to the single-junction device. The bilayer device reached a higher PCE of 28.21%, benefiting from broader light absorption and enhanced charge generation capabilities. The external quantum efficiency (EQE) curve in Figure 3.5 reveals that the bilayer structure provides enhanced absorption particularly in the 860 -1260 nm wavelength range. This enhancement is primarily due to the $RbSnBr_3$ top absorber, which has a wider bandgap energy (approximately 0.988 eV), thus extending the spectral response and enabling more efficient photon harvesting. A summary of the key photovoltaic parameters

including short-circuit current density (J_{sc}), open-circuit voltage (V_{oc}), fill factor (FF), and PCE for all simulated structures is provided in Table 3.2.

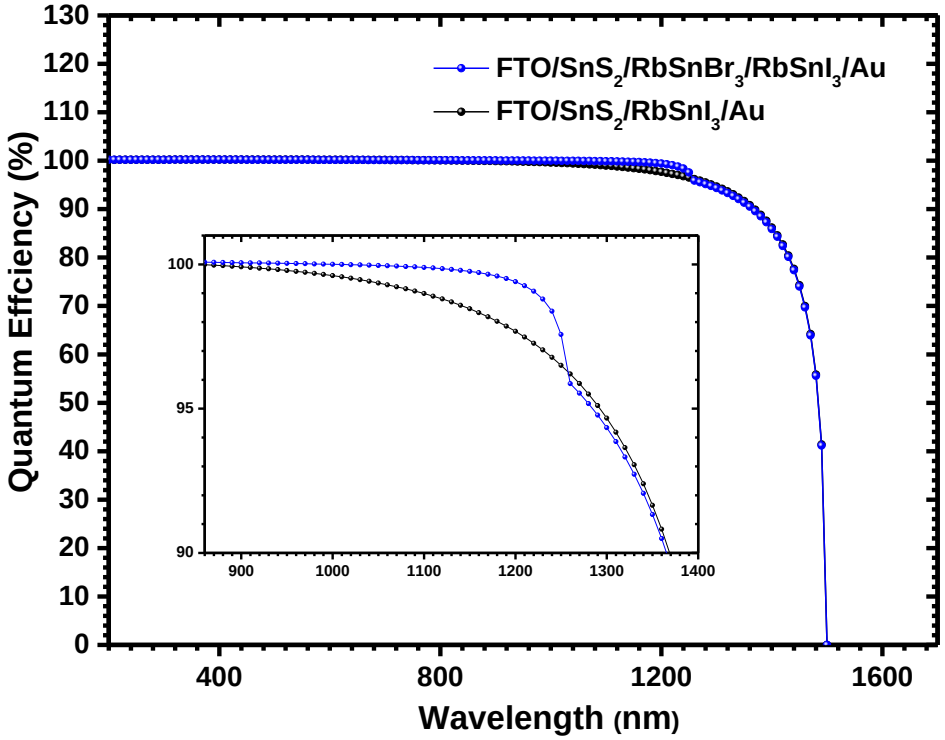

Figure 3.5: Comparison of Quantum Efficiency Characteristics between $RbSnI_3$ Single-Junction and $RbSnBr_3/RbSnI_3$ Bilayer PSCs.

Table 3.2: Photovoltaic Characteristics of Simulated $RbSnI_3$ and $RbSnBr_3/RbSnI_3$ Bilayer PSCs.

Device configuration	J_{sc} (mA/cm^2)	V_{oc}(V)	*FF* (%)	*PCE* (%)
FTO/ SnS_2/C_{60}/ $RbSnI_3$/Au (Simulation) [3]	51.57	0.63	81.48	26.38
FTO/SnS_2/ $RbSnI_3$/Au (This work)	51.83	0.63	81.45	26.50
FTO/SnS_2/ $RbSnBr_3$/ $RbSnI_3$/Au (This work)	51.86	0.72	75.81	28.21

3.3.1. Optimization of $RbSnBr_3/RbSnI_3$ bilayer PSC

In this section, we introduce optimization strategies for the $RbSnBr_3/RbSnI_3$ bilayer perovskite solar cell (PSC) to enhance its overall performance.

3.3.1.1. Selection of a suitable ETL for bilayer PSC

The selection of an appropriate electron transport layer (ETL) is a critical step in designing an efficient solar cell. In this analysis, eight different ETL materials were investigated and compared. These include SnS_2, WS_2, CdS, $Cd_{0.5}Zn_{0.5}S$, $BaSnO_3$, ZnSe, ZnS_2, and In_2S_3. The material parameters used for each ETL in the numerical simulations are listed in Table 3.3.

Table 3.3: Material Parameters Used in SCAPS Simulation for Different ETL Candidates [4-8].

Parameters	ETLs						
	$BaSnO_3$	**WS_2**	**ZnS_2**	**In_2S_3**	**ZnSe**	**$Cd_{0.5}Zn_{0.5}S$**	**CdS**
E_g (eV)	3.16	1.87	2.24	2.1	2.81	2.8	2.4
χ_e (eV)	3.9	4.3	4.24	4.65	4.09	3.8	4.18
E_{ps}	17	11.9	10	13.5	8.6	10	10
μ_n (cm^2/Vs)	200	20	50	400	400	100	260
μ_p (cm^2/Vs)	25	10	50	210	110	25	51
N_v (cm^{-3})	1.8×10^{19}	2.4×10^{19}	1.8×10^{19}	4×10^{13}	1.8×10^{18}	1×10^{18}	2.4×10^{19}
N_c (cm^{-3})	1.2×10^{19}	1×10^{19}	2.2×10^{18}	1.8×10^{19}	2.2×10^{18}	1×10^{18}	1×10^{19}
N_d (cm^{-3})	1×10^{16}	1×10^{16}	1×10^{16}	1×10^{16}	1×10^{16}	1×10^{16}	1×10^{16}
N_a (cm^{-3})	-	-	-	-	-	-	-
N_t (cm^{-3})	1×10^{14}	1×10^{14}	1×10^{14}	1×10^{14}	1×10^{14}	1×10^{14}	1×10^{14}

As shown in Table 3.4, the simulation results reveal that the CdS ETL exhibits the highest power conversion efficiency (PCE) of 28.36%, outperforming the other ETL candidates. The conduction band offset (CBO) plays a vital role in determining electron transfer efficiency at the absorber/ETL interface. A negative CBO value facilitates smooth electron flow; however, it may lead to increased recombination at the interface, particularly in the presence of high defect densities. Therefore, minimizing interface defects is crucial for optimizing device performance [12]. Although materials such as SnS_2, WS_2, ZnSe, and ZnS_2 are compatible with the bilayer design and provide good performance, CdS was selected as the optimal ETL due to its slightly superior efficiency.

Table 3.4: Electrical performance comparison of various ETLs in the $RbSnBr_3/RbSnI_3$ Bilayer PSC structure.

ETLs	J_{sc} (mA/cm^2)	V_{oc}(V)	*FF* (%)	*PCE* (%)
SnS_2	51.86	0.72	75.81	28.21
WS_2	51.86	0.69	75.61	27.14
CdS	51.86	0.72	75.59	28.36
Cd0.5Zn0.5S	51.84	1.09	22.57	12.70
$BaSnO_3$	51.87	0.72	57.15	21.46
ZnSe	51.86	0.72	75.27	28.25
ZnS_2	51.86	0.72	75.77	28.15
In_2S_3	51.81	0.62	72.20	23.06

3.3.1.2. Optimization of $RbSnI_3$ bottom absorber layer

After selecting CdS as the most suitable ETL, we investigated the effect of the $RbSnI_3$ bottom absorber layer's doping concentration and thickness on the performance of the bilayer PSC. The doping concentration was varied from 10^{12} to 10^{20} cm^{-3}, and the thickness (t_m) was varied between 100 nm and 1500 nm. Figure 3.6 illustrates the variation in device performance with changes in the doping concentration $N_A(RbSnI_3)$. The power conversion efficiency (PCE) remains nearly constant at around 28.30% for low doping levels (10^{12} to 10^{16} cm^{-3}). However, beyond 10^{16} cm^{-3}, the efficiency starts to increase gradually, peaking at 34.86% when the doping reaches 10^{20} cm^{-3}. This enhancement is mainly attributed to improved charge collection efficiency and reduced carrier recombination. However, excessively high doping concentrations may cause the material to lose its semiconducting behavior and approach metallic characteristics. Therefore, an optimal doping concentration of 10^{18} cm^{-3}, which results in a PCE of 30.80%, was selected for further analysis.

Figure 3.7 shows the efficiency trend as a function of the $RbSnI_3$ absorber thickness, $t_m(RbSnI_3)$, while keeping the doping concentration fixed at 1×10^{16} cm^{-3}. The PCE increases with thickness up to 500 nm, beyond which it begins to decline. This trend indicates that a 500 nm thickness provides the best balance between light absorption and carrier collection, yielding a maximum efficiency of 30.87%. As a result, 500 nm was chosen as the optimal thickness for the $RbSnI_3$ bottom absorber layer in the remainder of this study.

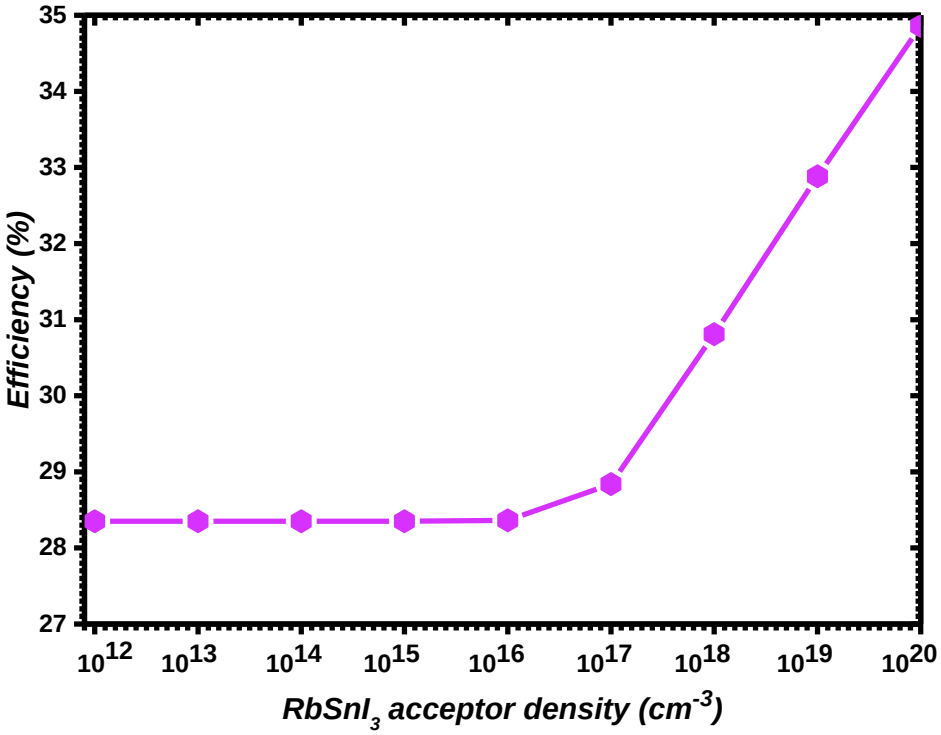

Figure 3.6: *Power Conversion Efficiency as a Function of $RbSnI_3$ Doping Concentration.*

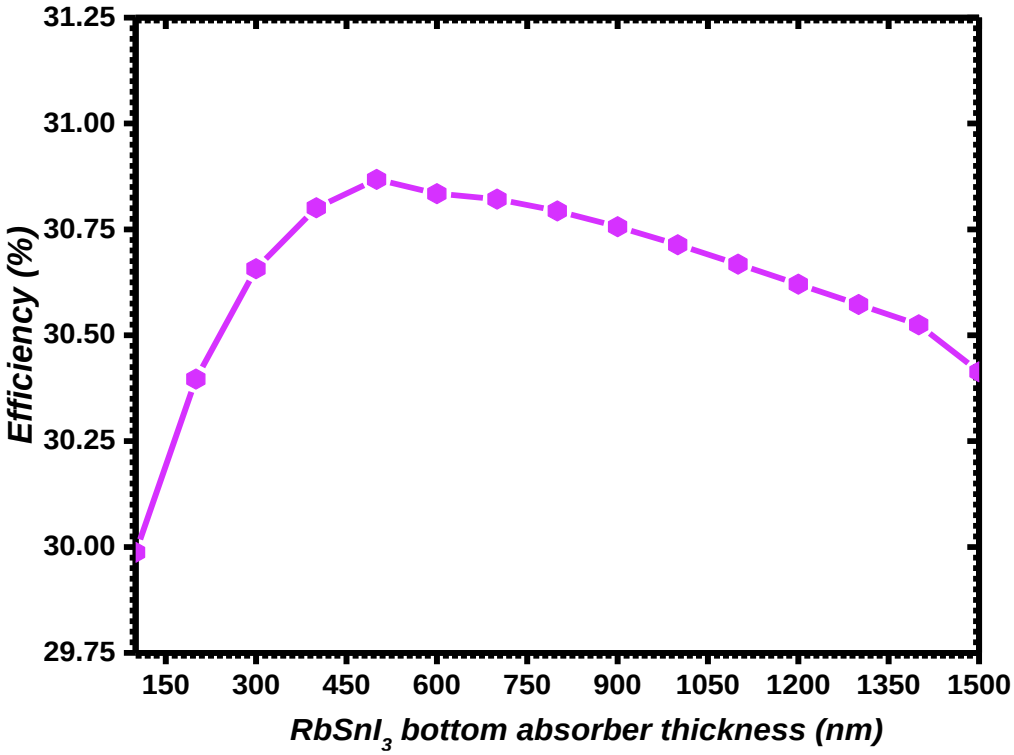

Figure 3.7: *Power Conversion Efficiency as a Function of $RbSnI_3$ Absorber Layer Thickness.*

3.3.1.3. Optimization of $RbSnBr_3$ top absorber layer

After optimizing the $RbSnI_3$ bottom absorber layer, we then investigated the effect of the $RbSnBr_3$ top absorber layer's doping concentration and thickness on the performance of the bilayer PSC, following a similar approach. The acceptor doping concentration was varied from 10^{12} to 10^{20} cm^{-3}, and the thickness (t_m) from 100 nm to 1500 nm. Figure 3.8 illustrates the variation in device performance with changes in the doping concentration $N_A(RbSnBr_3)$. The efficiency remained almost stable in the doping range between 10^{12} and 10^{17} cm^{-3}, reaching a maximum value of approximately 31.37% at a concentration of 10^{18} cm^{-3}. Beyond this point, the efficiency gradually declined, with a sharp drop observed at 10^{20} cm^{-3}. Thus, the optimal doping concentration was determined to be 1×10^{18} cm^{-3}.

Figure 3.9 shows the efficiency trend as a function of the $RbSnBr_3$ absorber thickness, $t_m(RbSnBr_3)$, with the doping concentration fixed at 1×10^{18} cm^{-3}. The efficiency increases slightly up to a thickness of 1000 nm, beyond which it saturates. Therefore, a thickness of 1000 nm is considered sufficient for optimal performance, achieving a PCE of approximately 31.40%.

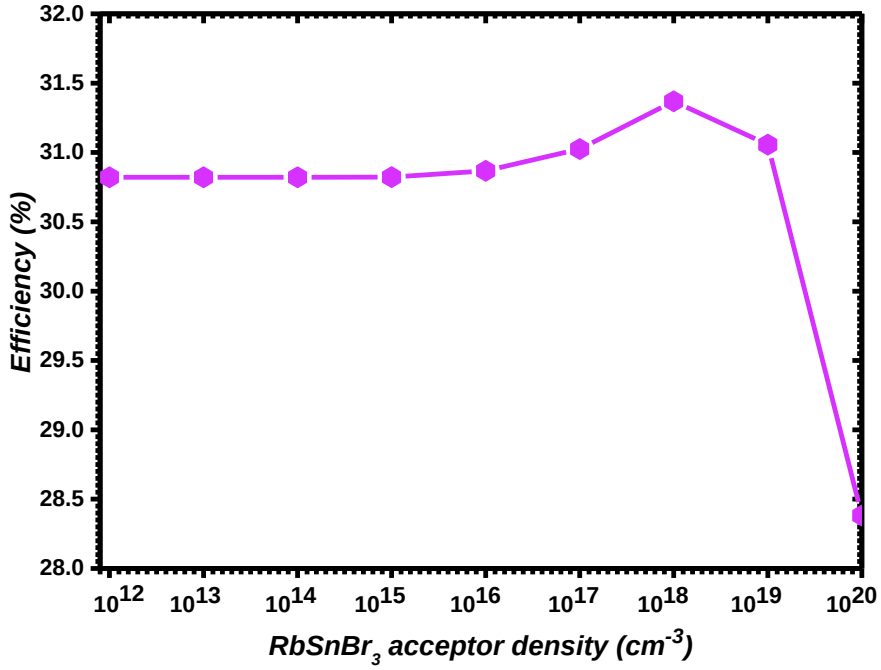

Figure 3.8: *Power Conversion Efficiency as a Function of $RbSnBr_3$ Doping Concentration.*

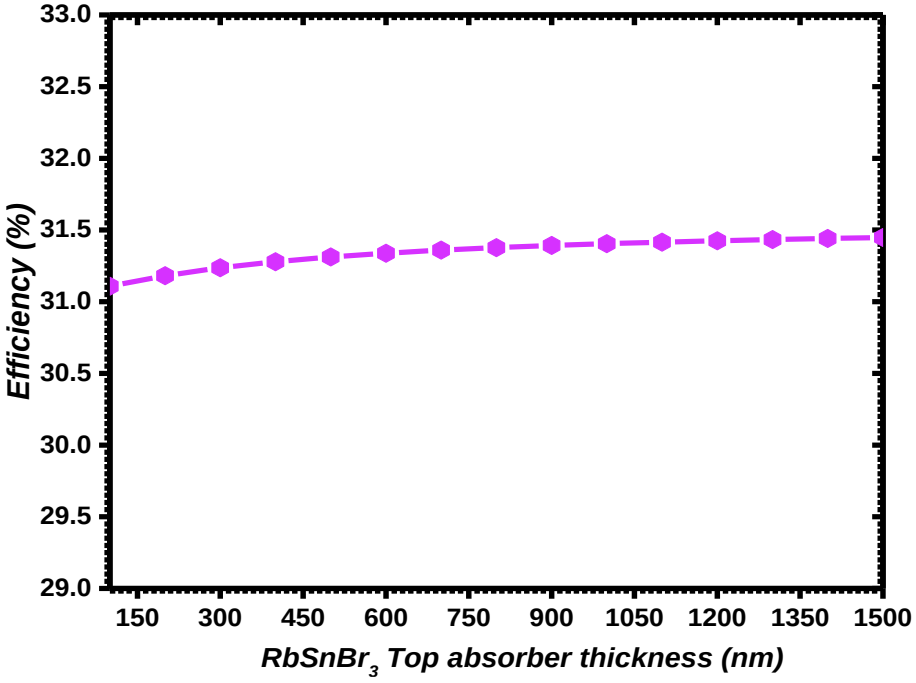

Figure 3.9: *Power Conversion Efficiency as a Function of $RbSnBr_3$ Top Absorber Layer Thickness.*

3.3.1.4. Optimization of CdS ETL layer

Using the optimal parameters obtained in the previous sections for both the bottom ($RbSnI_3$) and top ($RbSnBr_3$) absorber layers, we next investigated the effect of the CdS (ETL) on the performance of the bilayer PSC. Specifically, we varied the donor doping concentration and thickness of the CdS layer to evaluate their influence on device efficiency. The donor concentration

N_D(CdS) was varied over a range from 10^{12} to 10^{20} cm^{-3}. Figure 3.10 shows that the efficiency remains nearly constant between 31.40% and 31.50% across this entire doping range. This indicates that the donor concentration has a negligible impact on the photovoltaic performance. Consequently, we retained the same doping level used in the initial simulations, which is $1\times10^{16}cm^{-3}$.

In contrast, the thickness of the CdS layer had a more pronounced effect. As illustrated in Figure 3.11, the device efficiency gradually decreases with increasing CdS thickness, falling from its maximum at 20 nm down to significantly lower values at 500 nm. This efficiency reduction is likely due to the increased optical absorption by the CdS layer, which reduces the number of photons reaching the bilayer absorber layers. Therefore, it is advantageous to use a thinner CdS ETL layer to enhance photocurrent generation [13]. Based on the results, the optimal thickness for the CdS ETL layer is determined to be 20 nm.

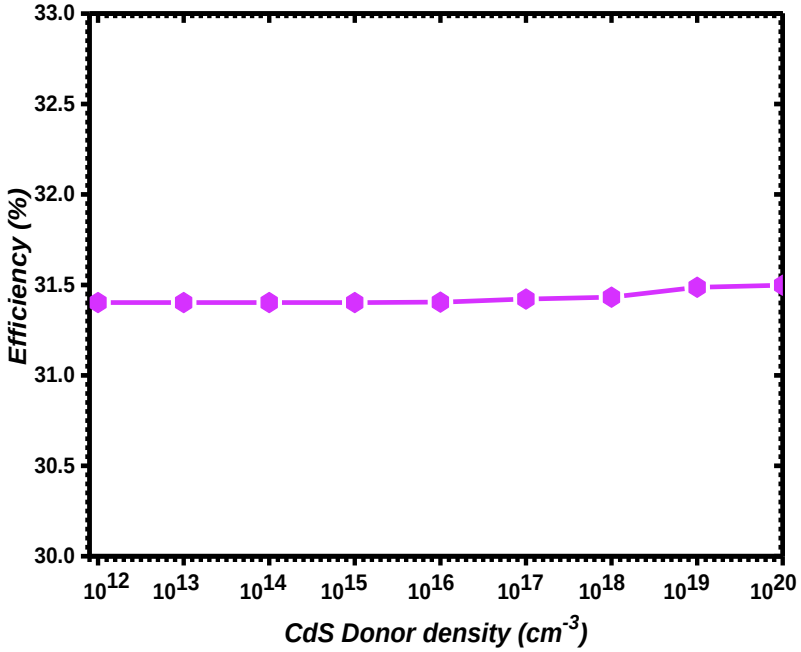

Figure 3.10: *Power Conversion Efficiency as a Function of CdS Doping Concentration.*

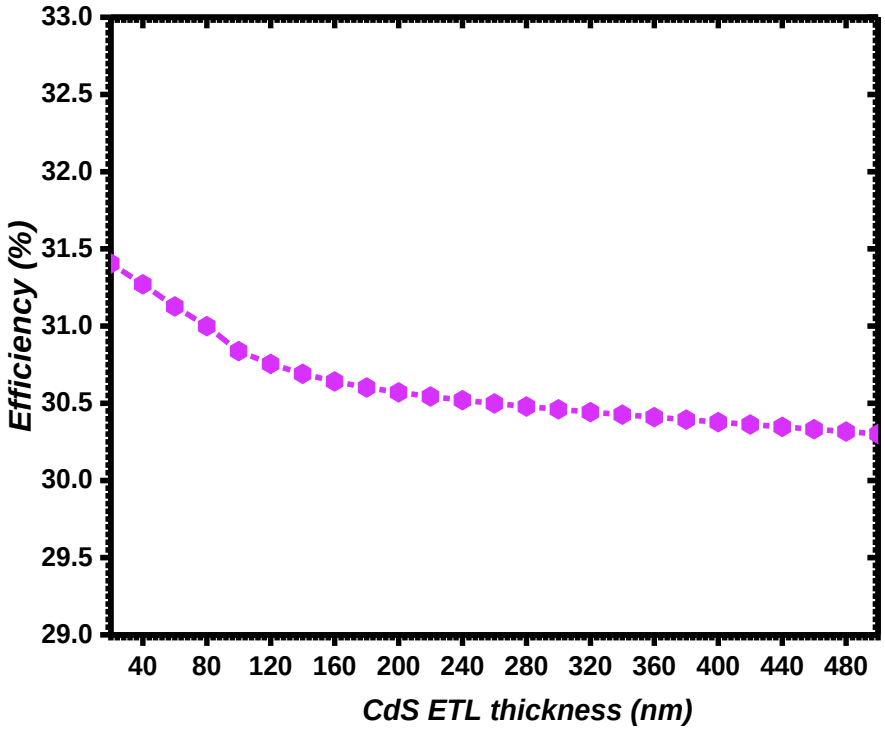

Figure 3.11: *Power Conversion Efficiency as a Function of CdS Layer Thickness.*

3.3.1.5. Analyzing the Impact of back contact metal

Finally, the influence of different back contact metals on the efficiency of the bilayer PSC was analyzed by evaluating the effect of metal work function. Various metals with differing work functions were considered as alternatives to gold (Au), and their impact on device performance was assessed. The selected metals and their corresponding work functions are: iron (Fe, 4.81 eV), carbon (C, 5.0 eV), tungsten (W, 5.22 eV), nickel (Ni, 5.5 eV), palladium (Pd, 5.6 eV), and selenium (Se, 5.9 eV) [14]. As illustrated in Figure 3.12, metals with low work functions, such as Fe, result in a significant reduction in efficiency (26.87%). However, when the work function exceeds approximately 5.0 eV, there is a sharp increase in efficiency, which stabilizes around 31.40% for metals such as C, W, Ni, Pd, and Se. This performance enhancement can be attributed to the improved band alignment at the metal/perovskite interface. When a metal with a higher work function is used, the Fermi level shifts downward, reducing the Schottky barrier and promoting the formation of an ohmic contact [38]. This facilitates better charge extraction and minimizes recombination losses. Therefore, selecting a back contact metal with a high work function is essential for achieving optimal solar cell performance. Gold (Au), which was initially used in this design, demonstrates excellent compatibility and ensures both high efficiency and device stability. However, considering cost-effectiveness, lower-cost alternatives such as W, Ni, or C can also be viable options for practical implementation.

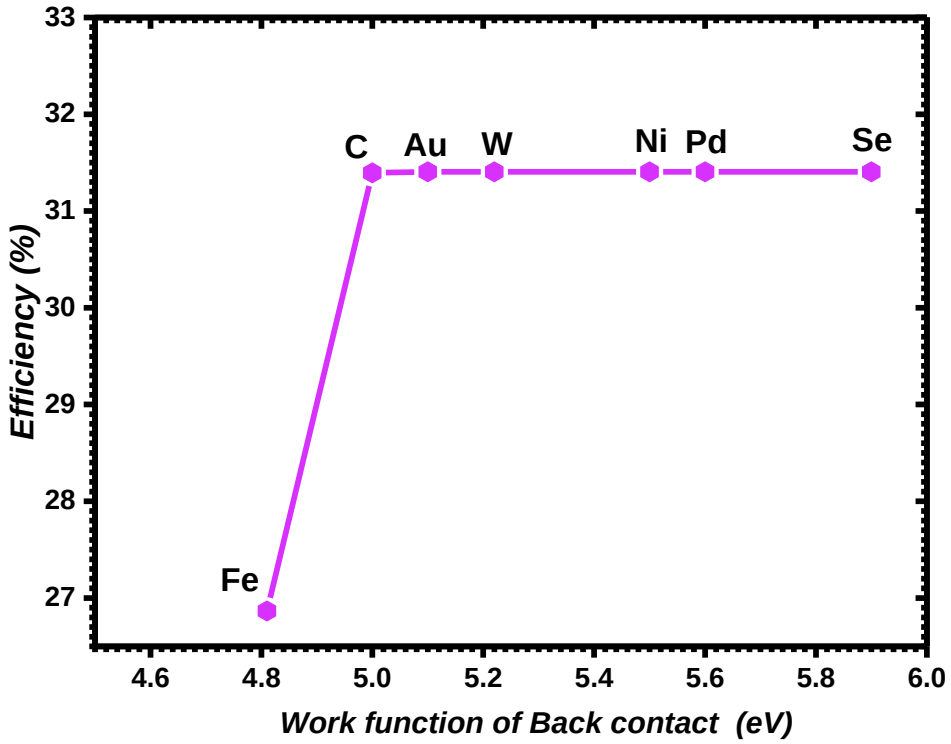

Figure 3.12: *Effect of back contact metal work function on the power conversion efficiency of the bilayer perovskite solar cell*

3.3.2. Optimum design

Based on the optimized results obtained in the previous sections, the best-performing structure was derived by incorporating the optimal parameters into the simulation model. The efficiency of the solar cell significantly increased after this improvement process, as illustrated in Figure 3.10, when compared to the bilayer cell before optimization. The final optimized design includes CdS as the most suitable ETL, along with the optimal thickness and acceptor doping concentration for the absorber layers. Specifically, the $RbSnI_3$ bottom absorber was set at a thickness of 500 nm and a doping concentration of $N_A = 1\times10^{18}$ cm^{-3}, while the $RbSnBr_3$ top absorber was fixed at 1000 nm with the same doping concentration ($N_A = 1\times10^{18}$ cm^{-3}). In addition, the CdS ETL layer with a thickness of 20 nm and a donor concentration of $N_D = 1\times10^{16}$ cm^{-3}. The current-voltage (J–V) characteristics shown in Figure 3.13 compare the performance of three solar cells: the single-junction device, the unoptimized bilayer structure, and the optimized bilayer structure. The optimized bilayer design (FTO/CdS/$RbSnBr_3$/$RbSnI_3$/Au) demonstrates the highest open-circuit voltage, short-circuit current, and fill factor, confirming the enhancement in PCE. Table 3.5 summarizes the key performance metrics of each structure, revealing an optimum efficiency of 31.40% for the optimized bilayer solar cell.

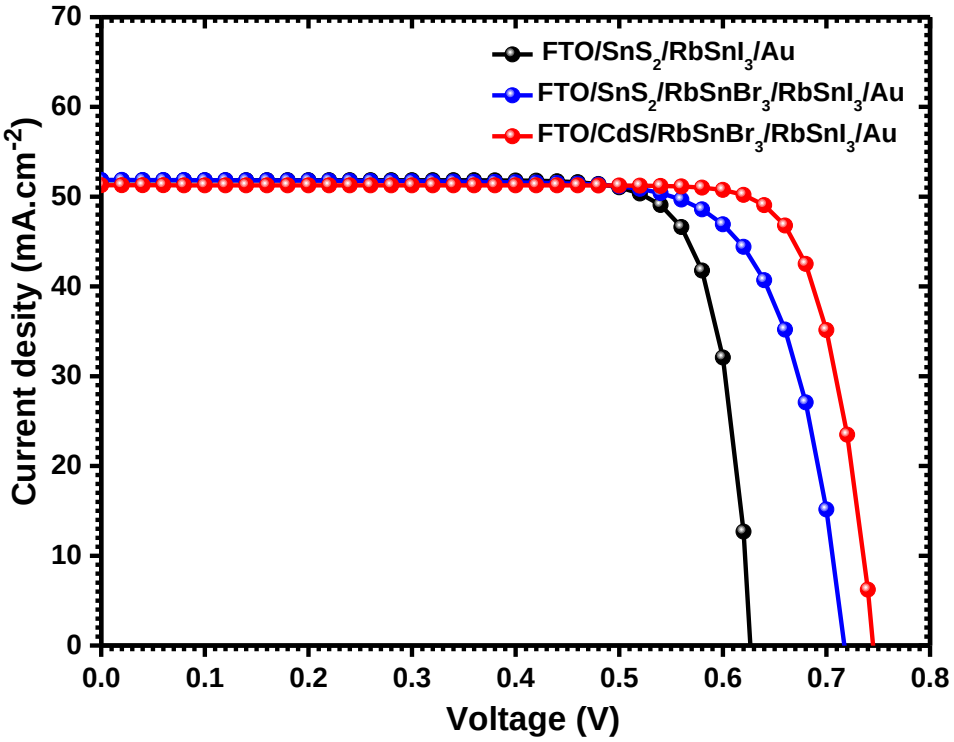

Figure 3.13: *Comparison of J–V Characteristics for $RbSnI_3$ Single-Junction PSCs and $RbSnBr_3$/$RbSnI_3$ Bilayer PSCs. (before and after optimization).*

Table 3.5: Photovoltaic Characteristics of Simulated $RbSnI_3$ and $RbSnBr_3$/$RbSnI_3$ Bilayer PSC (before and after optimization).

Device configuration	J_{sc} **(mA/cm^2)**	V_{oc}**(V)**	***FF*** **(%)**	***PCE*** **(%)**
$RbSnI_3$ Single-junction PSC	51.83	0.63	81.45	26.50
$RbSnBr_3$/ $RbSnI_3$ Bilayer PSC	51.86	0.72	75.81	28.21
$RbSnBr_3$/ $RbSnI_3$ Bilayer PSC (optimized)	51.27	0.75	82.15	31.40

3.4.Conclusion

In this chapter, we conducted a detailed numerical investigation of single-layer and bilayer perovskite solar cells using SCAPS-1D. Beginning with the replication of a reference single-junction device—FTO/SnS_2/$RbSnI_3$/Spiro/Au—we validated the accuracy and reliability of our simulation setup by achieving results consistent with those previously published.

Recognizing the limitations in efficiency of the single-absorber structure, we proposed a bilayer configuration by incorporating $RbSnBr_3$ as a top absorber layer, resulting in the stacked bilayer structure FTO/SnS_2/$RbSnBr_3$/$RbSnI_3$/Spiro/Au. Comparative analysis clearly demonstrated the performance enhancement offered by the bilayer design, particularly in terms of improved light absorption and charge collection.

To further enhance device performance, we undertook a systematic optimization of key parameters, including the selection of an appropriate electron transport layer (ETL), fine-tuning the thickness and doping concentrations of both absorber layers, and evaluating the influence of various back contact metals. This parametric study led to the identification of an optimal device configuration that maximizes power conversion efficiency while maintaining material compatibility and practical feasibility.

The findings of this chapter not only underscore the benefits of bilayer architectures for lead-free perovskite solar cells but also provide a clear pathway for further development and experimental realization. These results will serve as the foundation for future work aimed at bridging the gap between simulation and practical device fabrication.

References Chapter 3:

[1] Counter Electrode Material Selection for Dye-Sensitized Solar Cells: A Review" ،C. Karunakaran *Journal of Materials Science: Materials in Electronics* ،2017.

[2] Li, D., He, X., Zhang, X., Chen, J., Jin, Q., & Xu, J. (2024). Investigating Ultrafast Electron Transfer in Graphene and Its Derivatives Composites by Femtosecond Transient Absorption Spectroscopy. *ChemPhotoChem*, *8*(7), e202300271.

[3] Harun-Or-Rashid, M., Rahman, M. F., Amami, M., Farhat, L. B., Islam, M. M., & Benami, A. (2025). Exploring new lead-free halide perovskites RbSnM3 (M= I, Br, Cl) and achieving power conversion efficiency> 32%. *Journal of Physics and Chemistry of Solids*, *197*, 112437.

[4] Singh, N., Agarwal, A., & Agarwal, M. (2024). Computational investigation of lead-free NaZn0· 7Ag0. 3Br3 based double-perovskite solar cell. *Journal of Physics and Chemistry of Solids*, *193*, 112140.

[5] Pindolia, G., Shinde, S. M., & Jha, P. K. (2022). Optimization of an inorganic lead free RbGeI3 based perovskite solar cell by SCAPS-1D simulation. *Solar Energy*, *236*, 802-821.

[6] Ming, C., Zhou, H., Wu, J., Hu, C., Fan, W., Ma, X., ... & Qiao, S. (2023). The design and performance optimization of all-inorganic CsPbIBr2/CsSnI3 heterojunction perovskite solar cells. *Solar Energy*, *263*, 111885.

[7] Reza, M. S., Rahman, M. F., Kuddus, A., Reza, M. S., Monnaf, M. A., Islam, M. R., ... & Ezzine, S. (2024). Improving the efficiency of a new perovskite solar cell based on Sr3SbI3 by optimizing the hole transport layer. *Energy & Fuels*, *38*(3), 2327-2342 .

[8] Reza, M. S., Rahman, M. F., Kuddus, A., Mohammed, M. K., Al-Mousoi, A. K., Islam, M. R., ... & Hossain, M. K. (2023). Boosting efficiency above 28% using effective charge transport layer with Sr 3 SbI 3 based novel inorganic perovskite. *RSC advances*, *13*(45), 31330-31345.

[9] Sheehan, S., Surolia, P. K., Byrne, O., Garner, S., Cimo, P., Li, X., ... & Thampi, K. R. (2015). Flexible glass substrate based dye sensitized solar cells. *Solar Energy Materials and Solar Cells*, *132*, 237-244.

[10] Reza, M. S., Rahman, M. F., Kuddus, A., Mohammed, M. K., Al-Mousoi, A. K., Islam, M. R., ... & Hossain, M. K. (2023). Boosting efficiency above 28% using effective charge transport layer with Sr 3 SbI 3 based novel inorganic perovskite. *RSC advances*, *13*(45), 31330-31345.

[11] Harun-Or-Rashid, M., Farhat, L. B., Brahmia, A., Mohammed, M. K., Rahman, M. A., Azzouz-Rached, A., & Rahman, M. F. (2024). Analysis of the role of A-cations in lead-free A3SbI3 (A= Ba, Sr, Ca) perovskite solar cells. *Journal of Materials Science*, *59*(15), 6365-6385.

[12] Singh, N. K., & Agarwal, A. (2023). Performance assessment of sustainable highly efficient CsSn0. 5Ge0. 5I3/FASnI3 based Perovskite Solar Cell: A numerical modelling approach. *Optical Materials*, *139*, 113822.

[13] Tinedert, I. E., Saadoune, A., Bouchama, I., & Saeed, M. A. (2020). Numerical modelling and optimization of CdS/CdTe solar cell with incorporation of Cu2O HT-EBL layer. *Optical Materials*, *106*, 109970.

[14] Tinedert, I. E., Saadoune, A., & Hossain, M. K. (2024). A theoretical study of all-inorganic perovskite solar cells: computational modeling of the CsPbI3/RbGeI3 bilayer absorber structure. *Journal of Physics and Chemistry of Solids*, *189*, 111951.

General conclusion

General Conclusion

In conclusion, this study investigated the performance of single-absorber perovskite solar cells (PSCs) based on $RbSnI_3$, as well as the enhancement achieved by incorporating $RbSnBr_3$ to form a bilayer absorber architecture, using the SCAPS-1D simulation tool. The results demonstrated that the $RbSnBr_3/RbSnI_3$ bilayer structure significantly outperforms the single-absorber counterpart due to its broadened absorption spectrum and improved charge carrier separation. Through a detailed evaluation of various electron transport layers (ETLs), CdS was identified as the most suitable material, yielding superior performance in the bilayer configuration. Furthermore, the efficiency of the bilayer PSCs was notably improved by systematically optimizing key parameters, including absorber layer thickness and acceptor doping concentrations. The optimal configuration was achieved with an $RbSnBr_3$ top absorber thickness of 1000 nm and an acceptor density of 1×10^{18} cm^{-3}, combined with an $RbSnI_3$ bottom absorber thickness of 500 nm and the same acceptor density. Additionally, the influence of the back contact metal work function on device performance was investigated. It was found that when the work function exceeds approximately 5.0 eV, the cell performance improves and stabilizes. This provides viable alternatives to gold, such as carbon (C), tungsten (W), nickel (Ni), palladium (Pd), and selenium (Se), which may reduce fabrication costs while maintaining high efficiency.

Overall, the findings of this thesis underscore the strong potential for efficiency enhancement in lead-free perovskite solar cells through thoughtful design and material selection. These results contribute to the advancement of environmentally friendly and high-performing PSC technologies. We hope that this work will inspire further research and innovation in the development of sustainable solar energy solutions and the realization of next-generation photovoltaic devices.